Roughness of fault surfaces over nine decades of length scales

T. Candela, F. Renard, Y. Klinger, K. Mair, J. Schmittbuhl, E. E. Brodsky

Roughness of fault surfaces over nine decades of length scales

Thibault Candela,[1,2] François Renard,[1,3] Yann Klinger,[4] Karen Mair,[3] Jean Schmittbuhl,[5] and Emily E. Brodsky[2]

Received 19 November 2011; revised 6 June 2012; accepted 11 June 2012; published 11 August 2012.

[1] We report on the topographic roughness measurements of five exhumed faults and thirteen surface earthquake ruptures over a large range of scales: from 50 μm to 50 km. We used three scanner devices (LiDAR, laser profilometer, white light interferometer), spanning complementary scale ranges from 50 μm to 10 m, to measure the 3-D topography of the same objects, i.e., five exhumed slip surfaces (Vuache-Sillingy, Bolu, Corona Heights, Dixie Valley, Magnola). A consistent geometrical property, i.e., self-affinity, emerges as the morphology of the slip surfaces shows at first order, a linear behavior on a log-log plot where axes are fault roughness and spatial length scale, covering five decades of length-scales. The observed fault roughness is scale dependent, with an anisotropic self-affine behavior described by four parameters: two power law exponents H, constant among all the faults studied but slightly anisotropic ($H_{\parallel} = 0.58 \pm 0.07$ in the slip direction and $H_{\perp} = 0.81 \pm 0.04$ perpendicular to it), and two pre-factors showing variability over the faults studied. For larger scales between 200 m and 50 km, we have analyzed the 2-D roughness of the surface rupture of thirteen major continental earthquakes. These ruptures show geometrical properties consistent with the slip-perpendicular behavior of the smaller-scale measurements. Our analysis suggests that the inherent non-alignment between the exposed traces and the along or normal slip direction results in sampling the slip-perpendicular geometry. Although a data gap exists between the scanned fault scarps and rupture traces, the measurements are consistent within the error bars with a single geometrical description, i.e., consistent dimensionality, over nine decades of length scales.

Citation: Candela, T., F. Renard, Y. Klinger, K. Mair, J. Schmittbuhl, and E. E. Brodsky (2012), Roughness of fault surfaces over nine decades of length scales, *J. Geophys. Res.*, *117*, B08409, doi:10.1029/2011JB009041.

1. Introduction

[2] Faults appear most commonly as more or less continuous linear breaks at the surface of the Earth, and their traces show wavy irregularities at all scales [*Brown and Scholz*, 1985]. These irregularities, which we call roughness, control the geometry [*Power et al.*, 1987], mechanics, and transport properties of fault zones [*Power and Durham*, 1997] and contribute to their 3D architecture [*Bistacchi et al.*, 2010; *Faulkner et al.*, 2010]. Fault roughness may control several faulting processes and parameters such as the total resistance to slip, the aseismic versus seismic behavior [*Voisin et al.*, 2007], the alteration of shear resistance during sliding, the magnitude of stress concentration and heterogeneity in the fault zone [*Chester and Fletcher*, 1997; *Chester and Chester*, 2000; *Schmittbuhl et al.*, 2006; *Candela et al.*, 2011a, 2011b], and the deformation and damage of the rock on either side of the fault [*Johnson and Fletcher*, 1994; *Dieterich and Smith*, 2009; *Griffith et al.*, 2010]. Other studies have also shown the importance of non-planar structures in the rupture propagation [*Nielsen and Knopoff*, 1998; *Aochi and Madariaga*, 2003] and the close relationship between the rupture geometry and its propagation velocity [*Vallée et al.*, 2008; *Bouchon et al.*, 2010].

[3] As direct observations are not possible at the depths of earthquake nucleation, surface roughness data from exhumed fault scarps [*Power et al.*, 1987; *Renard et al.*, 2006; *Sagy et al.*, 2007; *Candela et al.*, 2009; *Brodsky et al.*, 2011, and references therein] or earthquake surface ruptures [*Wesnousky*, 2006, 2008; *Klinger*, 2010] have been used to characterize fault plane morphology over a wide range of spatial scales.

[4] Pioneering studies that measured 2-D profiles on exhumed scarps found that their roughness cannot be described by a single number such as the standard deviation of the roughness amplitude. Rather, fault surface topography was measured as self-affine fractal with the amplitude of the

[1]ISTerre, University of Grenoble I, CNRS, OSUG, Grenoble, France.
[2]Department of Earth and Planetary Sciences, University of California, Santa Cruz, California, USA.
[3]Physics of Geological Processes, University of Oslo, Oslo, Norway.
[4]Institut de Physique du Globe de Paris, Sorbonne Paris Cité, UMR 7154, CNRS, Université Paris Diderot, Paris, France.
[5]Institut de Physique du Globe de Strasbourg, UMR 7516, CNRS, Strasbourg, France.

Corresponding author: T. Candela, ISTerre, University of Grenoble I, CNRS, OSUG, BP 53, F-38041 Grenoble, France. (thibault.candela@ujf-grenoble.fr)

0148-0227/12/2011JB009041

topography increasing with the wavelength under consideration. A 2-D rough profile (Figure 1) is self-affine if it remains statistically invariant under the scaling transformation $\delta x \rightarrow \lambda \delta x$, $\delta z \rightarrow \lambda^H \delta z$ [*Feder*, 1988; *Meakin*, 1998], where δx is the coordinate along the 2-D profile, δz the roughness amplitude and H the Hurst exponent (or roughness exponent). If the power law scaling exponent $H \neq 1$, different magnification factors will be needed in the directions parallel and perpendicular to the profile for a small portion of the profile to appear statistically similar to the entire profile (Figure 1). If $H < 1$, the slope at large scales along a self-affine profile scales as $s = \delta z/\delta x \propto \delta x^{H-1}$, and tends to flatten for long wavelengths, suggesting a significant role of the small spatial scales [*Schmittbuhl et al.*, 1995a]. Since the exponent H does not contain any information on the amplitude of the signal, and is related only to the progression in space, a second parameter is needed to describe fully the power law: the amplitude of the scaling behavior. In this study, we call this parameter the pre-factor of the power law, which determines the magnitude of the surface roughness at a given scale [*Mandelbrot*, 1983, p. 350; *Power and Tullis*, 1991].

[5] Recently, with the development of a new generation of 3-D laser scanners, fast and accurate acquisitions of topographic data are now available, allowing more fault surfaces to be characterized [*Renard et al.*, 2006; *Sagy et al.*, 2007; *Candela et al.*, 2009; *Brodsky et al.*, 2011] in contrast to discrete 2-D profiles. In the present study, we investigate roughness properties of five fault surfaces using three independent scanner devices (a Light Detection And Ranging apparatus – also called LiDAR, a laser profilometer, and a white light interferometer), together spanning a range of scales from 5×10^{-5} m to 10 m. A focus of our study is to include measurements at different scales on the same fault surface by physically sampling large, exposed surfaces to extract samples for laboratory analyses. Our prior data on fault surface roughness [*Candela et al.*, 2009; *Angheluta et al.*, 2011; *Candela et al.*, 2011a, 2011b] have been updated and extended with new measurements (see Tables 1a and 1b). We present also here new results on the geometry of thirteen map-scale rupture traces of large continental earthquakes (see Table 2), giving access to a range of scales from 200 m to 50 km. Both map-scale rupture traces and scanned fault surfaces include multiple geological contexts in terms of lithology, tectonic regime, and the accumulated slip. Our data set, gathering together measurements of exhumed faults and ruptures traces, provides an opportunity to investigate the geometrical/topological properties of the fault surfaces over a range of spatial scales from 5×10^{-5} m to 50 km.

[6] In order to evaluate these properties, we characterize the self-affine scaling of both data sets (scanned fault surface and rupture traces) using the same statistical tool, *i.e.* the Fourier power spectrum analysis. This is a robust technique well-suited for characterizing self-affine roughness of fault zones [*Candela et al.*, 2009]. A self-affine topographic model implies that the Fourier spectrum of the roughness, plots as a linear trend in log-log coordinates as a function of either the spatial frequency or wavelength. Two parameters describe such a self-affine model in the spectral domain: the slope of the power spectrum (directly proportional to H) and its pre-factor (i.e., the intercept at a given length scale) on a log-log plot of the Fourier spectrum. Both parameters are necessary and sufficient to describe a self-affine geometry. We compute these two parameters for the fault surfaces and rupture traces in order to decipher if a global tendency emerges and/or to characterize the fluctuations.

[7] After detailing our data set (Section 2) and the roughness analysis method (Section 3), we will show in Section 4 that a single anisotropic self-affine description best fits the roughness properties of the exhumed fault scarps. In addition, the earthquake rupture traces are characterized by a self-affine exponent equal to that of the exhumed fault surfaces in the slip-perpendicular direction. Finally, in Section 5 we discuss the possibility that a single anisotropic self-affine geometrical description is maintained from the micrometric scale to the map-scale earthquake surface rupture.

2. Fault Roughness Data

2.1. Exhumed Fault Scarps

[8] We have analyzed five natural fault surfaces which were selected because of their particularly well preserved slip surfaces, large exposures and few pits or weathering damage patterns. Existing data sets on the Vuache-Sillingy [*Candela et al.*, 2009; *Angheluta et al.*, 2011], Magnola [*Candela et al.*, 2009], Corona Heights [*Candela et al.*, 2011a], Dixie Valley [*Candela et al.*, 2011b] faults have been updated with new measurements and extended with the Bolu fault (see Tables 1a and 1b). As examples, two fault surfaces (Corona Heights fault, Figure 2 and Bolu fault, Figure 3) have been selected to illustrate the topographic data with the three scanner devices covering complementary scales. These fault surfaces are composed of many discrete slip surfaces delimiting bumpy lenses elongated in the direction of slip (Figure 2). These multiscale bumpy lenses give the wavy aspect of the fault surfaces that are overprinted by fine linear polished striations and coarser corrugations generated by abrasions (Figures 2 and 3). A complete list of our fault data, including GPS locations, nature of the rock, direction of motion, and estimated finite geological slip, is given in Table 1a. The finite geological slip is always the most difficult of these parameters to estimate. In fact, if the total slip of a fault zone can be estimated from the displacement of geological markers, this total slip could have occurred on the several parallel slip surfaces constituting the fault zone, making it difficult to estimate the slip on a given slip surface. For each of our five scanned surfaces, we will consider a range of slips bracketed by the extreme values: the total slip of the fault zone and a minimum slip accommodated by individual surfaces. For example, the total geological slip of the North Anatolian fault was estimated equal to 85 $\pm$ 25 km [*Hubert-Ferrari et al.*, 2002], but it is not easy to define the slip accommodated specifically on each individual sub-parallel slip surface constituting the fault zone of the Bolu segment. Paleo-seismological investigations on the Bolu segment give a lower bound of approximately 20 m [*Kondo et al.*, 2005, 2010]. Similarly, although the total slip for the Corona Heights fault zone as a whole could be large (>1000 m), individual surfaces have recorded smaller ($\sim$1 m) displacements which are difficult to precisely estimate because of the absence of well-defined structural markers.

[9] The Corona Heights and Dixie Valley faults cut through silicate rocks. The Dixie Valley (Basin and Range province in Nevada) fault has a mainly normal slip component and

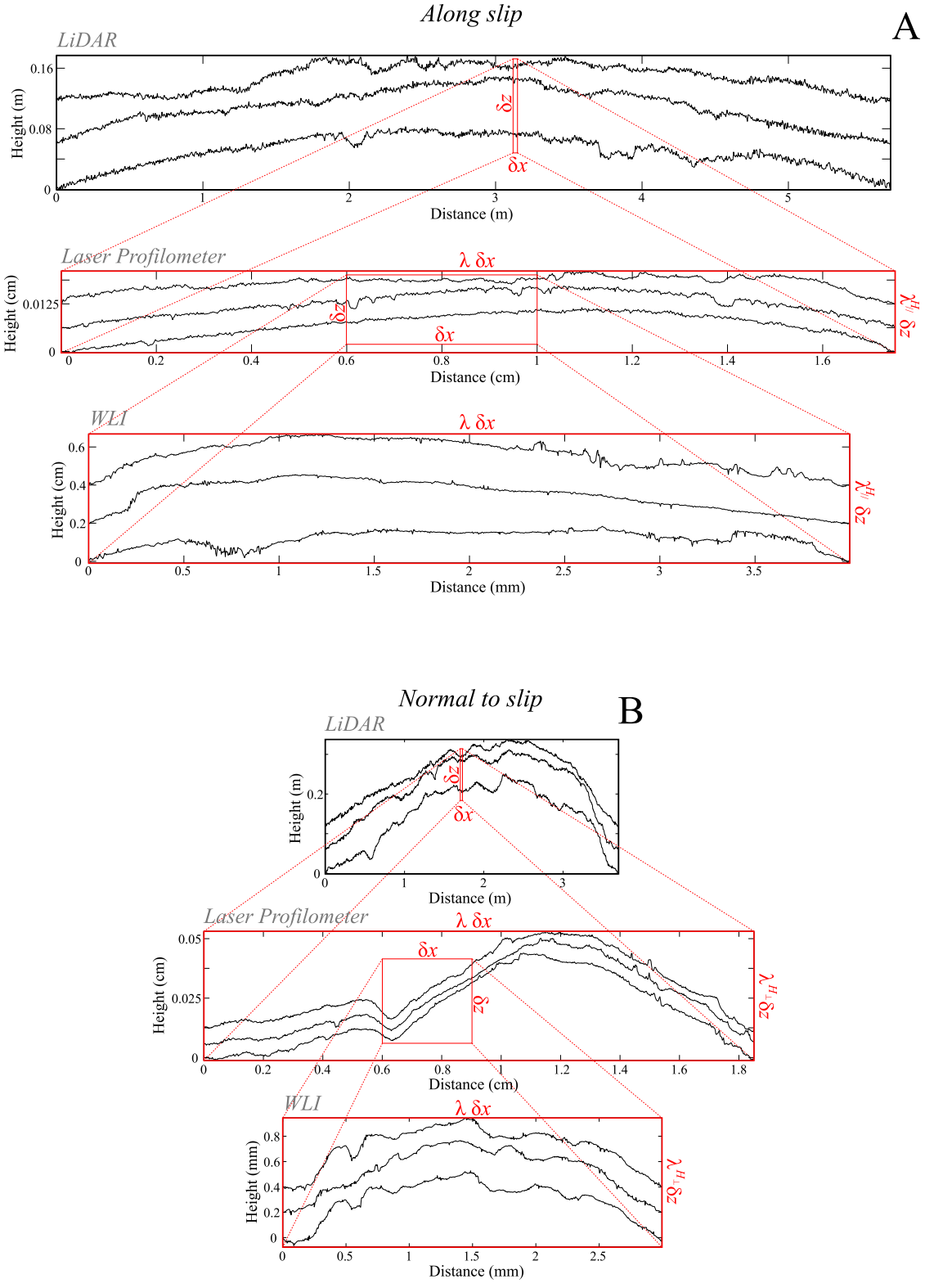

Figure 1. Roughness profiles from the Corona Heights fault surface in directions parallel and perpendicular to slip. (a) Profiles parallel to the slip direction and (b) perpendicular to the slip direction. A magnified portion of the profiles has a statistically similar appearance to the entire profiles when using the scaling transformation $\delta x \rightarrow \lambda \delta x$, $\delta z \rightarrow \lambda^{H_{\parallel,\perp}} \delta z$. Profiles have been shifted vertically for clarity.

Table 1a. Scanned Faults

Fault Name	Location	Lithology	Sense	Slip[a]
Vuache-Sillingy, France	45°57′14.5″N 6°2′56″E	Limestone	Strike-slip	10–30 m
Corona Heights, California	37°45′55″N 122°26′14″E	Chert	Strike-slip	Several m to >1 km
Bolu, Turkey	40°41′07″N 31°34′04″E	Limestone	Strike-slip	20 m to 85 km
Dixie Valley, Nevada	39°56′48″N 117°56′43″E	Rhyolites	Normal	Several m to 3–6 km
Magnola, Italy	42°7′N 13°28′31″E	Limestone	Normal	Several m to >500 m

[a]Except for the Vuache-Sillingy fault surface, a lower and upper bound of the slip is given. Although total geological cumulated slip for the fault zone as a whole can be kilometric (*i.e.* the upper bound), scanned individual surfaces within the fault zone may have experienced considerably less slip (i.e., the lower bound).

Table 1b. Laser Scanner Characteristics and Fault Roughness Results[a]

								Average	
Fault Name	Fault Patches	Scanner	δx[b]	Spatial Precision	δz[c]	$H_{\parallel}$	$H_{\perp}$	$H_{\parallel}$	$H_{\perp}$
Vuache-Sillingy	Surf-1	GS 100 (Trimble)	20 mm	±5 mm	4.5 mm	0.60[d,e,g]	0.78[d,g]	0.60 ± 0.07	0.81 ± 0.02
	Surf-7	GS 100 (Trimble)	20 mm	±5 mm	4.5 mm	0.68[d,e,g]	0.82[d,g]		
	Surf-6	LMS Z420i (Riegl)	30 mm	±7.5 mm	10.2 mm	0.50[d,e,g]	0.82[d,g]		
	Surf-JPG	S10 (Trimble)	1 mm	±0.25 mm	0.9 mm	0.63[d,e]	0.83[d]		
	Small	Lab. profilo-meter	20 μm	±1 μm	<1 μm	0.65[d,e]	0.81[d]	0.61 ± 0.05	0.80 ± 0.01
	Vu-1-G					0.57[h]	0.80[h]		
	Vu-A-1	WLI	2 μm	±0.025 μm	3 nm	0.58[e]	0.76[h]	0.60 ± 0.04	0.79 ± 0.03
	Vu-A-2		2 μm			0.55[e]	0.78[h]		
	Vu-A-7		1 μm			0.65[e]	0.84[h]		
	Vu-A-8		1 μm			0.61[h]	0.79[h]		
Corona Heights	Corona-A	HDS 3000 Leica	5 mm	±1.25 mm	2 mm	0.57[f]	0.85[h]	0.65 ± 0.04	0.83 ± 0.03
	Corona-B					0.65[f]	0.81[h]		
	Corona-C					0.67[f]	0.87[h]		
	Corona-D					0.64[f]	0.81[h]		
	Corona-E					0.69[f]	0.79[h]		
	Corona-F					0.67[f]	0.85[h]		
	P3	Lab. profilo-meter	20 μm	±1 μm	<1 μm	0.66[f]	0.86[h]	0.63 ± 0.04	0.85 ± 0.03
	Co-AGU					0.60[f]	0.85[h]		
	Co-A-4	WLI	2 μm	±0.025 μm	3 nm	0.62[f]	0.82[h]	0.62 ± 0.03	0.83 ± 0.02
	Co-A-9		1 μm			0.63[f]	0.85[h]		
Bolu	Stack 2345	Ilris-3D Optech	20 mm	±5 mm	20 mm	0.48[h]	0.79[h]	0.50 ± 0.07	0.78 ± 0.02
	Stack67					0.50[h]	0.78[h]		
	Stack12					0.44[h]	0.78[h]		
	W-detail-2					0.45[h]	0.76[h]		
	E-detail-3					0.49[h]	0.80[h]		
	E-detail-2					0.46[h]	0.80[h]		
	E-detail-1					0.65[h]	0.74[h]		
	Bolu-1	Lab. profilo-meter	20 μm	±1 μm	<1 μm	0.58[h]	0.79[h]	0.55 ± 0.05	0.76 ± 0.04
	Bolu-2					0.51[h]	0.74[h]		
Dixie Valley	Dixie-1	HDS 3000 Leica	5 mm	±1.25 mm	2 mm	0.66[g]	0.79[g]	0.59 ± 0.08	0.82 ± 0.03
	Dixie-2					0.63[g]	0.80[g]		
	Dixie-3					0.61[g]	0.84[g]		
	Dixie-4					0.47[g]	0.84[g]		
	Map-1	Lab. profilo-meter	20 μm	±1 μm	<1 μm	0.57[h]	0.82[h]	0.59 ± 0.03	0.81 ± 0.03
	Map-2					0.61[h]	0.81[h]		
	Dixie-D	WLI	2 μm	±0.025 μm	3 nm	0.56[h]	0.88[h]	0.56 ± 0.05	0.88 ± 0.01
	Dixie-H		1 μm			0.50[h]	0.87[h]		
	Dixie-E		2 μm			0.61[h]	0.89[h]		
	Dixie-C		2 μm			0.59[h]	0.89[h]		
Magnola	A32	Ilris-3D Optech	20 mm	±5 mm	20 mm	0.59[d]	0.77[d]		
	M2	Lab. profilo-meter	20 μm	±1 μm	<1 μm	0.60[d]	0.83[d]		

[a]The raw data (in term of XYZ cloud of points) are available at http://isterre.fr/recherche/equipes/mecanique-des-failles/observatoires-et-plateforme-de/article/fault-morphology-database?lang=fr.
[b]Spatial length scale resolution (δx).
[c]Vertical resolution (δz).
[d]*Candela et al.* [2009].
[e]*Angheluta et al.* [2011].
[f]*Candela et al.* [2011a].
[g]*Candela et al.* [2011b].
[h]This publication.

Table 2. Characteristics and Roughness Results of Earthquake Rupture Maps Used in This Study[a]

Name and References	Year	Sense	Magnitude	Rupture Length (km)	Total Geological Slip[b] (km)	H_R	Pre-factor (m^3)
Owens Valley (USA) *Klinger* [2010]	1872	Strike-slip	M_w 7.5–7.8	81	≤20–30	0.6 ± 0.1	4×10^{-2}
Haiyuan (China) *Klinger* [2010]	1920	Strike-slip	M_s 8 to 8.7	200	15 to 95	0.8 ± 0.1	7×10^{-3}
Gobi-Altay (Mongolia) *Klinger* [2010]	1957	Strike-slip	M 8.3	235	2 to 20	0.7 ± 0.1	2×10^{-2}
Superstition Hills (USA) *Klinger* [2010]	1987	Strike-slip	M 6.6	18	≤24	0.7 ± 0.1	2×10^{-3}
Luzon (Philippine) *Klinger* [2010]	1990	Strike-slip	M_w 7.8	107	50 to 200	0.8 ± 0.1	1×10^{-2}
Landers (USA) *Klinger* [2010]	1992	Strike-slip	M_w 7.2	65	3.1 to 4.6	0.8 ± 0.1	1×10^{-3}
Zirkuh (Iran) *Klinger* [2010]	1997	Strike-slip	M_w 7.2	104	60	0.9 ± 0.1	3×10^{-4}
Hector mine (USA) *Klinger* [2010]	1999	Strike-slip	M_w 7.1	39	3.4	0.7 ± 0.1	7×10^{-3}
Kashmir (Pakistan) *Kumahara and Nakata* [2006]	2005	Thrust	M_w 7.6	51	1.85 to 2.3	0.7 ± 0.1	9×10^{-2}
Chi-Chi (Taiwan) *Chen et al.* [2001]	1999	Thrust	M_w 7.6	76	≥12	0.9 ± 0.1	2×10^{-2}
Wenchuan (China) *Xu et al.* [2009]	2008	Thrust	M_w 7.9	249	8.6 to 17.3	0.8 ± 0.1	2×10^{-2}
Hebgen Lake (USA) *Myers and Hamilton* [1964]	1959	Normal	M_s 7.5	11	0.305	0.7 ± 0.1	6×10^{-2}
Borah Peak (USA) *Crone and Machette* [1984]	1983	Normal	M_s 7.3	19.5	≥2.5	0.8 ± 0.1	3×10^{-2}

[a]The raw data (in terms of XZ profiles) are available at http://isterre.fr/recherche/equipes/mecanique-des-failles/observatoires-et-plateforme-de/article/fault-morphology-database?lang=fr.
[b]References for each earthquake are given in the text.

crosscuts through rhyolite. Chemical changes during faulting at depth have altered the mineralogy and chemical composition of the rock in the fault zone [*Power et al.*, 1987; *Power and Tullis*, 1989, 1992]. The material that forms the fault consists almost entirely of secondary quartz, a mineral which is extremely resistant to weathering and allows extremely good preservation of the slip surfaces. Using gravity studies combined with reflection seismology studies [*Okaya and Thompson*, 1985], *Power and Tullis* [1989] estimate that the total normal slip is probably between 3 and 6 km. Geological and mineralogical constraints indicate that the slickenside surface formed at depths of less than 2 km and temperatures less than 270°C [*Power and Tullis*, 1989]. Major historical earthquakes and microearthquakes occurred on the region of the studied fault scarp [*Wallace and Whitney*, 1984; *Doser*, 1986]. Additionally, *Power and Tullis* [1989] have argued that seismic faulting played a role in the development of the slickenside surfaces, based on textural features they described in the fault surface materials. The Corona Heights strike-slip fault (Figure 2), located in the Castro district of San Francisco, crosscuts brown Franciscan cherts and was exposed by post-1906 earthquake anthropogenic quarrying. The relatively recent exposure of the fault and the high resistance of cherts to weathering allows for excellent preservation of the slip surface (Figure 2).

[10] The other three faults offset limestone rocks (Vuache-Sillingy in the French Alps, Magnola in the Appenines, and Bolu in Turkey). The Vuache-Sillingy fault is an active strike-slip fault system in the western part of the French Alps and has accumulated a total slip in the kilometer range [*Thouvenot*, 1998]. The fault surface we analyzed lies on a short segment of this fault system, where the accumulated slip was small, in the range of 10–30 meters, as estimated on aerial photographs. The fault plane was exhumed in the 1990s by quarrying and, as a consequence, the LiDAR measurements were performed on fresh, vegetation free surfaces, where weathering is minimal. The Magnola fault [*Candela et al.*, 2009], in the Fuccineo area, is part of the extensive fault system in central Apennines, Italy. This 15 km long normal fault shows microseismic activity and presents an average vertical displacement larger than 500 meters. The site we study has been recently exhumed [*Palumbo et al.*, 2004; *Carcaillet et al.*, 2008] with less alteration by weathering than older exhumed portions of the fault. The Bolu fault is part of the North Anatolian strike-slip fault system. The study area (Figure 3) is a part of the section that ruptured during the 1944 earthquake [*Kondo et al.*, 2005, 2010; *Barka*, 1996]. The small vertical component of the motion (~1 m), compared to the dominant horizontal strike-slip motion (~3.5 m), was responsible for the partial exhumation of the fault plane (Figure 3) during the 1944 earthquake [*Barka*, 1996]. More recently, anthropogenic activity (excavation for a garbage dump) also contributed to the exhumation of the outcrop.

[11] The five faults studied show slip activity during the Quaternary. The Bolu fault records both the propagation and termination of the 1944 earthquake. The Dixie Valley outcrop lies north of a segment that broke in 1954; it is the same outcrop studied by *Power et al.* [1987]. For three of these faults, the slip surfaces were exhumed recently by anthropogenic activity during the 20th century (Vuache-Sillingy, Bolu, and Corona Heights). These three surfaces were therefore exposed to atmospheric alteration for only a short period of time and therefore their roughness reflects only faulting processes. The Dixie Valley fault was exhumed by normal faulting activity combined with local quarrying. In this region, desert weather conditions and the silicate rocks result in slow chemical alteration. For this fault, we have chosen surfaces free of mechanical erosion, where the mirror-like polishing due to the latest slip activity was still present. Finally, the Magnola slip surfaces were those for which the alteration was the most significant. For this fault, we selected slip surfaces that were exhumed by Quaternary normal slip on the fault, and for which the erosion was minimal (*i.e.* surface away from a stream that could have increased the erosion rate); however we cannot discount that weathering has altered the roughness properties of these surfaces. We will show later that the roughness properties of the Magnola fault do not deviate significantly from those of the other faults and interpret this observation as evidence that weathering processes did not influence our roughness analyses at the spatial scales we considered.

[12] Even if it is difficult to accurately determine under which conditions at depth (confining pressure, temperature, strain rate and chemical environment) fault surfaces were built, the five fault studied here sample a range of different control parameters: slip accumulated (10 s of meters to ~10 s of kilometers), lithology (rhyolite, chert and limestone),

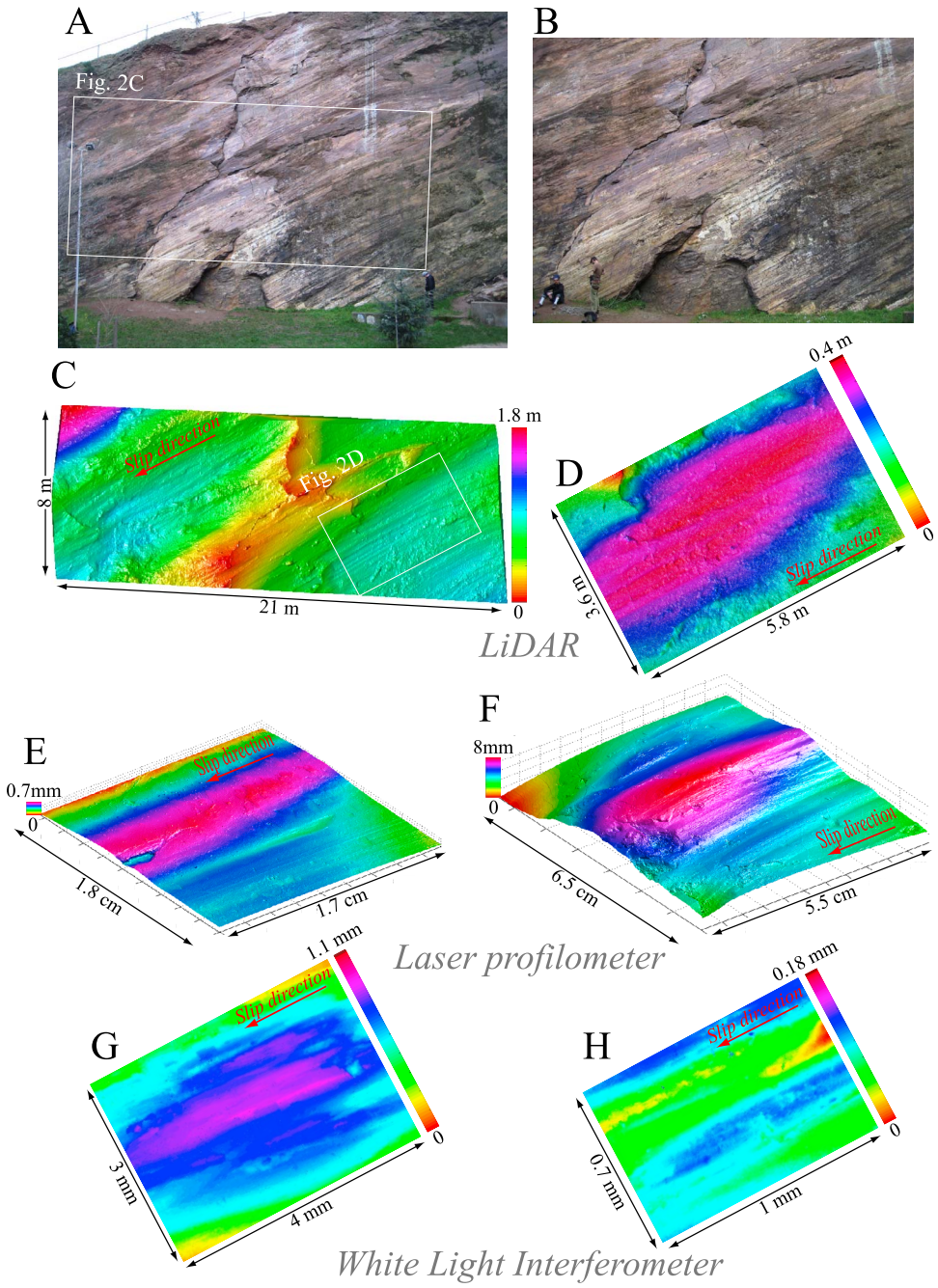

Figure 2. Corona Heights fault, California. Multiple bumpy discrete slip surfaces constituting lenses and striations can be detected at all scales, from the measurement resolution of each scanner device to the size of the entire exposure. (a) Whole outcrop view. The inset corresponds to the surface shown on Figure 2c. (b) Zoom on the fault showing different segments constituting the surface. (c, d) Map of fault surfaces scanned using LiDAR. The inset in C corresponds to the patch shown on Figure 2d. (e, f) Maps of fault surfaces scanned with the laser profilometer. (g, h) Zoom on the Figures 2e–2f scanned with the white light interferometer.

tectonic regime (strike-slip, oblique and normal) which possibly could have affected the fault surface roughness.

2.2. Scanner Devices and Digital Elevation Models of Fault Roughness

[13] Fault surface topography was scanned in the field using five different types of 3-D portable LiDAR laser scanners (see Table 1b) that use the time of flight of a light beam to accurately measure distances. The laser scanner records the topography of each exposed fault surface by collecting a cloud of points whose three dimensional coordinates correspond to points on the fault surface [*Renard et al.*, 2006; *Sagy et al.*, 2007; *Candela et al.*, 2009; *Resor and Mee*r, 2009; *Wei et al.*, 2010]. The actual point spacing

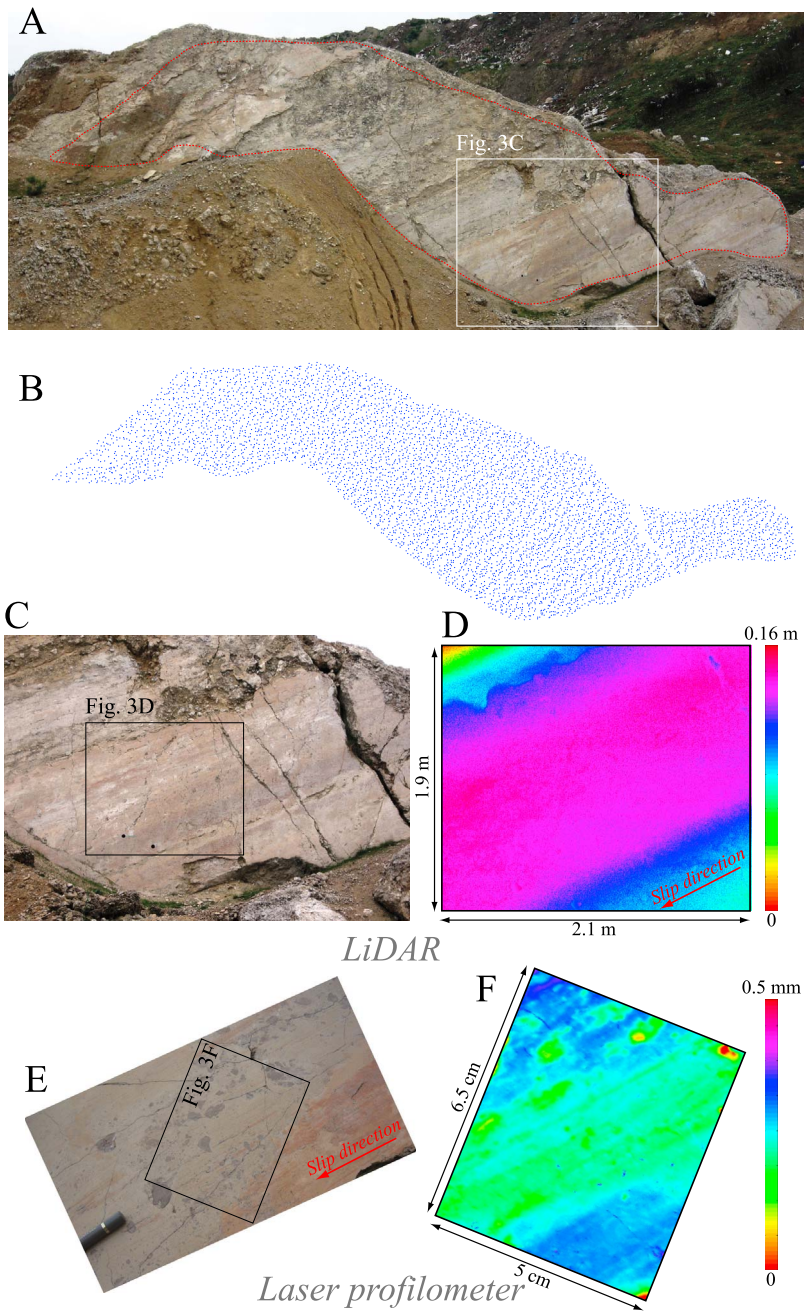

Figure 3. Bolu Fault, Turkey. (a) Photograph of the fault zone in the Bolu limestone. Dashed red contour corresponds to (b) the limits of the cloud of points. (c) Photograph of a well-preserved slip surface constituting the fault zone. (d) LiDAR data of surface displayed in Figure 3c. (e, f) Zoom on the fault surface and the corresponding topographic map acquired with the laser profilometer, which still includes anisotropic roughness features in the slip direction.

depends on the distance between the target and the scanner and a chosen angular spacing. For each fault outcrops, fresh sub-surfaces were selected and scanned for higher resolution acquisition (Figures 2 and 3).

[14] Our field data sets cover surface scales from 1 m^2 to 800 m^2 at a spatial length scale resolution δx from 1 mm to 30 mm. This spatial length scale resolution δx corresponds to the point spacing after the data processing (see Section 3), and is systematically taken to be twice as large as the average irregular spacing during the acquisitions, that is from 0.5 mm to 15 mm. The actual precision in the spatial positioning is estimated to be at most half the original average spacing, that is ± 0.25 mm to ± 7.5 mm. The height precision achievable depends on scanning conditions and is closely related to the spatial length scale resolution and to the roughness amplitude of the surface. In Table 1b, δz represents the estimated amplitude of the instrumental noise.

[15] The scans were combined with digital photographs to distinguish clear slip surfaces from eroded areas. This manual cleaning of the extremely large data sets (several tens of

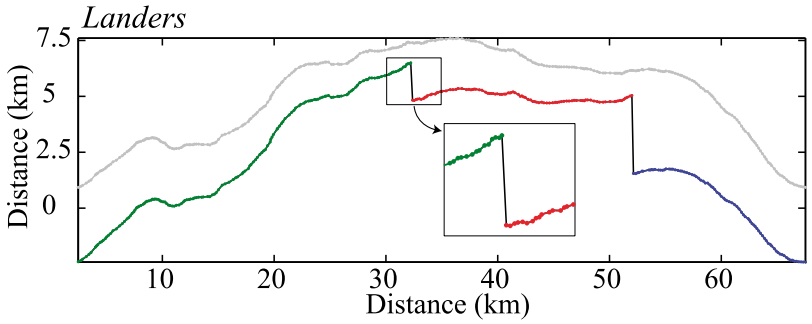

Figure 4. Digitized surface rupture trace of the three largest segments of the Landers earthquake. The data correspond to *Klinger* [2010, Figure 5g]. The inset zooms on one of the steps removed for the Fourier transform analysis. Each segment is individualized by different colors and the steps are represented in dark. The reconstructed trace by removing steps is displayed in gray.

millions of points) was completed using 3-D Reshaper software, a point cloud editor and visualization tool. Once all non-fault features such as trees, grass, or anthropogenic structures were removed, the whole fault scarp or selected smaller patches were analyzed (Figures 2 and 3). Typically, in our data sets, less than 5% of points were removed from the raw scanner data as spurious. As pointed out by *Candela et al.* [2009], the estimation of the fault surface properties was not significantly biased by the presence of randomly distributed holes and missing data in the cloud of points (see Appendix A1 for a quantitative analysis of the bias inherent to data acquisition in the estimation of the geometrical properties of fault surfaces).

[16] In the laboratory, we used a home-made laser profilometer [*Méheust*, 2002], to measure samples of the fault surfaces (between 200 mm^2 and 1000 mm^2, Figures 2 and 3), set on a 2-axis moving table. Each surface is scanned by geometric triangulation, measuring the distance between the sample and a laser head [*Schmittbuhl et al.*, 2008; *Candela et al.*, 2009]. One difference between the LiDAR and the profilometers is that with the laser profilometer, the data are regularly spaced. The spatial length scale resolution δx is equal here to the horizontal step, i.e., 20 microns. The actual precision in the spatial positioning is ± 1 micron and the vertical resolution (δz) is better than 1 micron. The reliability and accuracy of the cloud of points obtained with this laser profilometer required that only few spurious points were removed (less than 0.01%).

[17] At the millimeter scale, the topography of several slip surfaces (between 0.5 mm^2 and 40 mm^2, Figures 2 and 3) was measured using white light interferometry microphotography [*Dysthe et al.*, 2002]. This is done with a microscope that uses a broadband white light source and that is coupled to a Michelson interferometer. A reference arm creates interference fringes with maximum intensity at equal optical path lengths of the imaging beam and reference beam. By vertical movement of the sample and simultaneous image capturing, the interference, intensity envelope, and thereby the relative height of the imaged surface at each pixel is determined with a resolution of $\delta z = 3$ nm. The horizontal resolution depends on the lens used; for the highest magnification it is at the diffraction limit of white light, of about 0.5 micron. In the present study, we have selected horizontal steps (δx) between 1 and 2 microns (Table 1b). The actual precision in the spatial positioning is estimated to be ± 0.025 micron. As for data acquired with the laser profilometer, the clouds of points obtained are regularly spaced and only some spurious points have been manually removed. The whole suite of characteristics of the scanners devices and digital elevation models (spatial precision, resolution δx, noise on the data δz) used in this study are shown in Table 1b.

2.3. Earthquake Surface Rupture Data

[18] In contrast to the exhumed fault scarps presented in Section 2.1, where the 3-D roughness is characterized, surface rupture data at larger scales provide only 2-D measurements (Figure 4), since full fault surfaces are not accessible for direct measurement. In the present study, high resolution geological maps of large continental strike-slip earthquake surface ruptures, in various geological settings, were analyzed using the data set of *Klinger* [2010]; see for an example, *Klinger* [2010, Figure 5]. These eight digitized rupture traces have been acquired using field cartography that allows mapping of the geomorphologic traces of the rupture, combined with slip distributions and high resolution satellite images [*Klinger et al.*, 2005, 2006; *Klinger*, 2010]. The actual point spacing is irregular and its average is between 200 m and 1300 m. However, the precision of each point based on the combined field observations and high resolution satellite images is close to the meter-scale [*Klinger et al.*, 2005]. This last detail is crucial for interpreting a multimeter fine description of the roughness of the rupture trace. In addition to these high resolution digitized rupture traces of eight strike-slip earthquakes, we have also analyzed five additional rupture traces of earthquakes with a main vertical component of motion. The mapping of the thrust rupture traces could be biased at some locations by earthquake-induced landslides (e.g., Kashmir earthquake). We will show later that the roughness properties of the thrust rupture traces do not deviate significantly from those of the normal rupture traces and interpret this observation as evidence that this complication does not influence our roughness analyses at the spatial scales we considered.

[19] To avoid any bias due to local wiggles of the digitized rupture trace, the data set was re-sampled to ensure consistent spatial sampling, independent of the length of each rupture [*Klinger*, 2010]. This re-sampling procedure does not affect the Fourier transform computation and makes it possible to keep the scaling information of the rupture traces (see Appendix A3).

[20] Geometric irregularities (e.g., fault azimuth changes or bends), that are commonly observed along the surface ruptures, reflect the multiscale en-echelon pattern of the fault system, and range from a few hundred meters to several kilometers in size. Due to the presence of abrupt steps associated with relay zones, which influence the Fourier transform and therefore bias the roughness analysis, the ruptures traces are divided into individual segments (Figure 4). A reconstruction of the entire rupture trace can still be made when removing steps. Note that for some earthquake surface traces (e.g., Luzon, Superstition Hills, Hector Mine), no abrupt steps were detected and the whole rupture trace can be directly analyzed.

[21] For each earthquake, the surface rupture length, magnitude, and total geological slip are provided in Table 2. Of these three parameters, we note that the total slip of a fault is the least constrained. For Owens Valley fault [*Beanland and Clark*, 1994], the total slip was estimated to be ≤20–30 km. For the Haiyuan fault [*Zhang et al.*, 1987] it is in the range from 10 to 15 km [*Burchfiel et al.*, 1991] to 95 ± 15 km [*Gaudemer et al.*, 1995]. For the Gobi-Altay fault, the total displacement lies in the range of 2–20 km [*Kurushin et al.*, 1997]. For the Superstition Hills fault, the total slip is still debated and, by comparison with the nearby San Jacinto Fault, the total displacement is estimated to be less than 24 km [*Sharp*, 1967]. For the Luzon earthquake, the cumulative slip of the fault is in the range of 50–200 km [*Karig*, 1983; *Mitchell et al.*, 1986], and *Ringenbach et al.* [1993] noticed that because this fault is active since the beginning of the Pleistocene, the total slip should be smaller than 200 km. The Hector Mine and Landers earthquakes occurred on faults that are part of the East California Shear Zone that has a total slip close to 65 km [*Jachens et al.*, 2002]. The individual geological total slip for Landers (3.1 to 4.6 km) and Hector Mine (3.4 km) faults were estimated from the offset of magnetic anomalies [*Jachens et al.*, 2002]. Korizan (1979) and Zirkuh (1997) earthquakes occurred on the Abiz fault that accommodates 60 km of right lateral motion along the Sistan suture between Iran and Afghanistan [*Berberian et al.*, 1999]. The 1999 Chi-Chi earthquake was caused by rupture of the Chelungpu fault, one of the most prominent active thrust faults of Taiwan that accommodates more than 12 km of displacement [*Chen et al.*, 2001]. *Hussain and Yeats* [2009] indicate that probably all the displacement on the Balakot-Bagh fault, hosting the 2005 Kashmir earthquake, could have been accumulated in the past 400–500 000 years. Based on a shortening rate across the Balakot-Bagh fault of 4 mm/year [*Kaneda et al.*, 2008], and assuming a fault-dip of 30° [*Avouac et al.*, 2006], the total slip is around 1.85 to 2.3 km. The Borah Peak earthquake (1983) ruptured the River fault where the net slip displacement is at least 2.5 km on the basis of topographic and sedimentary arguments [*Crone and Machette*, 1984]. The Hebgen Lake earthquake struck on the en-echelon Hebgen Lake-Red Canyon fault where *Witkind* [1964] indicates net cumulative slip is about 305 m. The Mw 7.9 Wenchuan, China, earthquake mainly ruptured the Beichuan fault along the Longmenshan thrust belt at the eastern margin of the Tibetan Plateau. *Fu et al.* [2011] indicate that the amount of late Cenozoic shortening across the Longmenshan belt may be just 10–20 km. This shortening is accommodated by four main sub-parallel faults including the Beichuan fault. Assuming a fault-dip of 30°, the accumulated slip on the Beichuan thrust should be around 8.6 to 17.3 km.

3. Analysis of Scaling Properties of Roughness Data

[22] In this section we detail the procedure that was used to characterize the scaling properties of the scanned fault surface topography. The same approach was followed for the digitized earthquake surface ruptures since they are considered as rough profiles extracted along the fault surface.

[23] First, the original 3-D cloud of points (Figure 3) was transformed to 2-D (X, Y) + 1-D (Z) data set [*Renard et al.*, 2006; *Sagy et al.*, 2007; *Candela et al.*, 2009; *Wei et al.*, 2010] where the Z direction was approximately perpendicular to the mean fault plane (X, Y). A set of parallel cuts was taken through the cloud of points to obtain a series of thin bands of points striking at an angle θ from the X axis. The thickness of the bands of points is equal to the average spacing (X, Y) of the original raw data. Then, each band of points was projected to obtain a series of profiles with irregularly spaced points. Linear interpolation on a regular spacing was performed independently on all profiles to yield a set of heights $h(X_\theta)$, function of the coordinate X_θ along the cut. The regular spacing taken for the linear interpolation was systematically chosen to be twice as large as the average irregular spacing of the original profiles.

[24] To describe the scaling properties of these rough profiles (Figure 1), we searched for possible spatial correlations of the height fluctuations. Along each profile, we computed auto-correlation functions. If the auto-correlation function of a rough profile is a power law and scales as $\langle h(x+\delta x)h(x)\rangle - \langle h(x+\delta x)\rangle\langle h(x)\rangle \propto \delta x^{2H}$, then the rough profile is self-affine with H the Hurst exponent, if multiaffinity is excluded [*Schmittbuhl et al.*, 1995a]. One way to estimate the Hurst exponent is to compute the Fourier transform. This method is well-suited and robust for recognizing and characterizing self-affine roughness, as demonstrated by *Candela et al.* [2009]. The Hurst exponent H can be estimated from the Fourier power spectrum, which has a power law form for a 2-D self-affine profile [*Barabási and Stanley*, 1995; *Meakin*, 1998]. The steps in the procedure to compute the Fourier power spectrum of each profile are as follows: 1) First, the residual drift in the signal is removed in order to avoid any ramp artifact for the Fourier analysis (see *Schmittbuhl et al.* [1995b] for a quantitative analysis of this trend artifact). Indeed, adjusting the mean fault plane to the reference plane of the measuring device is always hard to determine a priori. In addition, even if corrections are possible a posteriori, trend suppression is non-trivial and complex. All length scales are involved in the faulting process, even very large ones, and therefore suppressing macroscopic information may influence the scale invariance analysis at large scales. For the following analyses, and as suggested by *Schmittbuhl et al.* [1995a], the trend has been defined simply as the line fit through the first and last point. 2) In order to ensure that there are no step functions at the end of the finite window, we apply a 3% cosine taper. Note that a taper function of 5 and 10% has been tested and the results appear robust (see Appendix A2). 3) The Fourier power spectrum $P(k)$, i.e., the square of the modulus of the Fourier transform, is calculated as a function of

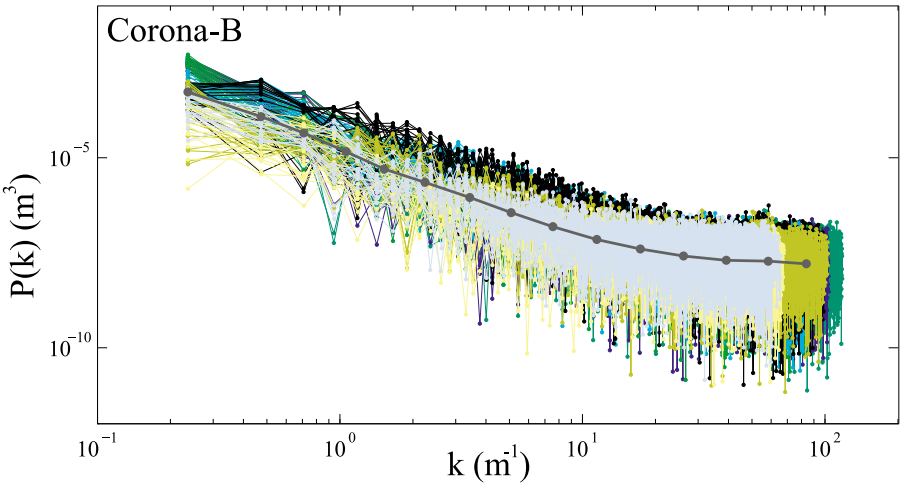

Figure 5. Average power spectrum of one LiDAR fault patch (Corona-B) obtained by averaging in a geometric progression (i.e., regularly spaced wave numbers in the log-log plot) several thousands 2-D power spectra of individual profiles. We have changed the color of the spectra every 20 profiles successively extracted from the surface.

wave number k. 4) The Fourier power spectrum is normalized by dividing the power at each wave number by the length of the profile. 5) Each cloud of points is computed as a whole by stacking and averaging all 2-D Fourier spectra to reduce the noise associated with individual profiles. In other words, for each cloud of points (fault patch), power spectral estimates with regularly spaced wave numbers are obtained by averaging the power spectra of the individual profiles in a geometric progression (Figure 5).

[25] As an example, the computed Fourier power spectra along the slip direction and perpendicular to it from patches of the Corona Heights fault surface acquired with each device (LiDAR, laser profilometer, WLI) are displayed in Figure 6. The uncertainty in the average spectral values obtained for each fault patch can be estimated following the method of *Bendat and Piersol* [1986]. This estimation of the uncertainty in the average spectral values assumes that the noise of each individual profile is uncorrelated with the noise of any of the other profiles. A one sigma confidence interval for the spectral power is given by:

$$\frac{\sqrt{n_s}\hat{P}(k)}{\sqrt{n_s}+1} \leq P(k) \leq \frac{\sqrt{n_s}\hat{P}(k)}{\sqrt{n_s}-1}$$

with $n_s(k) = n_y \Delta y\, k + 1$, where $P(k)$ and $\hat{P}(k)$ are the actual and calculated spectral power, respectively; n_y and n_s are the total number of profiles spaced a distance Δy apart perpendicularly to the profile direction, and the number of independent profiles used to calculate $\hat{P}(k)$, respectively. Note that n_s depends on scale. For the largest wave numbers, there are many more independent estimates of the total spectral power, and hence the error estimate is smaller than at the smallest wave numbers (see Figure 6).

[26] Note that for wavelengths below 50 mm, the fault surfaces we scanned with the LiDAR are so smooth that at this small scale, their spectral power falls within the range of those of the flat plate we use as a planar reference surface (Figure 6). That means that even if our LiDAR surface measurements were acquired at a spatial length scale resolution of 1 mm to 10 m (cf. Section 2.2), total power estimates of the surfaces are accurate only between 0.05 and 10 m scales. In contrast, the laser profilometer data and WLI data can be considered to be essentially noise free since their inherent noise level falls well below the magnitude of the fault surface topography (Figure 6).

[27] When plotting the average power spectrum as a function of wave number in a log-log space, a self-affine function reveals a linear slope, which is itself a function of H through $P(k) = C\, k^{-1-2H}$ (with C the pre-factor). Taking into account the possible uncertainties in the spectral power as previously described for our entire data set of fault surface patches, the upper limit of the error bar on the Hurst exponent estimated using a least square method is equal to ± 0.05 and does not vary significantly with the wave number. Due to the fact that only one rough profile for each rupture trace is analyzed (Figure 4), the noise in the spectrum is higher compared to the fault surface patch (constituted of an average of a multitude of profiles). For a single power spectral estimate, the standard deviation is equal to the mean [*Press et al.*, 2007]. So that the upper limit of the error bar in the estimated Hurst exponent of the eight rupture traces analyzed is equal to ± 0.1.

4. Fault Roughness Results

4.1. Roughness of Exhumed Fault Surfaces

[28] In order to extract the Hurst exponents characterizing the scaling behavior of the faults roughness, we have fit the linear part of each averaged spectrum obtained in the slip direction and perpendicular to it for each individual fault patch (Figure 6). Because we are interested in the variability of pre-factors, we have worked separately on each fault patch with each type of instrument instead of calculating average spectra for the full surface. We have focused our analysis on fault surface roughness between the largest scale accessible with the LiDAR, *i.e.* approximately 10 m, and to the scale of 0.05 mm accessible by the WLI. Figure 7 compiles all Hurst

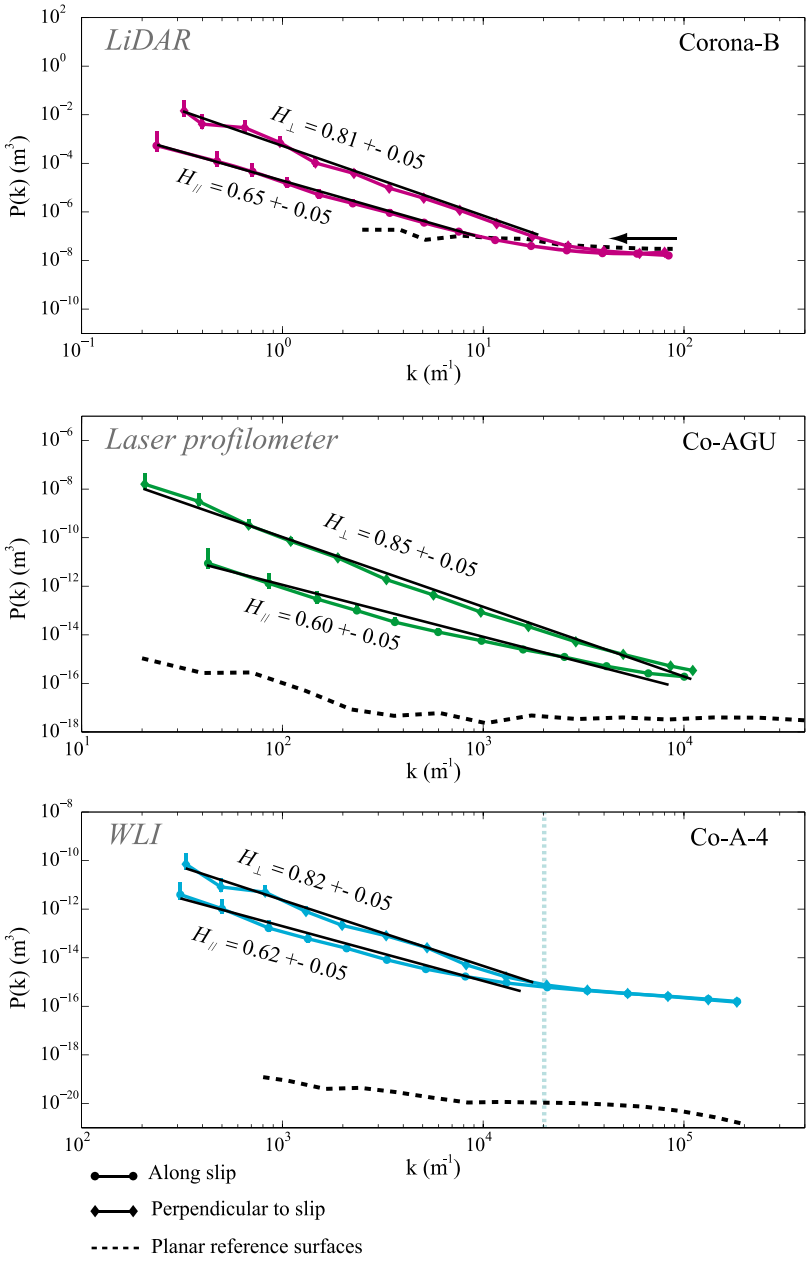

Figure 6. Typical average power spectra in the slip direction and perpendicular to it for fault patches scanned with the three devices used in our study. Error bars with 68% confidence interval (one sigma), and power law fits performed in linear portions of each average spectra, are shown. At the LiDAR scale, the black arrow indicates the lower limit used for the fits. This lower limit underlines the length scale at which spectra flatten out when they intersect the noise spectrum (black dashed line) calculated by scanning smooth, planar reference surfaces. For the laser profilometer and the WLI, the spectral power levels of our natural fault roughness data fall at a vertical higher position than the noise spectra (black dashed lines). However, at the WLI scale, the vertical dashed blue line at the bending of spectra indicates the lower limit of our fits. Even if this systematic change of slope at the length scale 0.05 mm seems to be related to intrinsic physical fault roughness properties, we arbitrarily limit our scaling analysis to scales larger than 0.05 mm.

exponents derived from each individual fault patch (41 subsurfaces in total) in the direction of slip and perpendicular to it. The five faults scanned can be characterized by two different global Hurst exponents between 0.05 mm and 10 m (see Table 1b): $H_{||} = 0.58 \pm 0.07$ in the direction of slip and $H_\perp = 0.81 \pm 0.04$ perpendicular to the slip. We will refer to $H_{||} = 0.6$ and $H_\perp = 0.8$ afterwards. This result highlights the fact that, for one direction (parallel or perpendicular to slip), the self-affine scaling of the relative amplitude of short and large wavelengths remains identical for the whole data set. In the data we present, fault surfaces with a Hurst exponent smaller or larger than one standard deviation of their distribution (± 0.07 in slip direction and ± 0.04 normal to slip) exist, but all Hurst exponents derived from our data fall

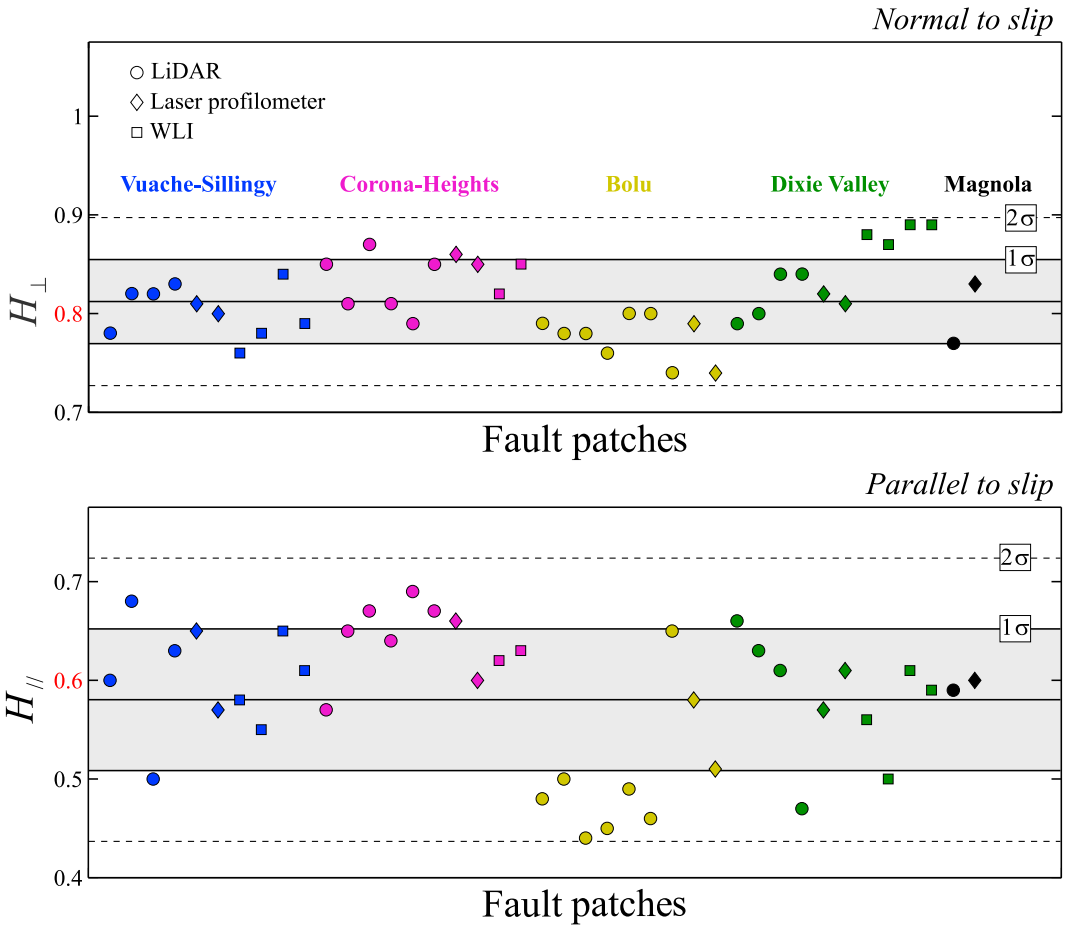

Figure 7. Plot of the Hurst exponents (see Table 1b) in direction (a) normal to slip and (b) parallel to it of the 41 scanned fault patches. The average Hurst exponent is equal to 0.58 along the direction of slip and 0.81 perpendicular to it. The shaded area and dashed lines indicate 1σ and 2σ confidence intervals, respectively.

within two standard deviations (Figure 7). Consequently, our global Hurst exponents appear to appropriately characterize the scaling behavior of the five faults studied when taking into account the fluctuations indicated in Table 1b.

[29] In addition, for each scanned fault patch, the along slip direction is smoother than perpendicular to it. This is seen by the lower position of power spectrum amplitudes for the along slip direction at each scale (Figure 6). More precisely, the power law relationships between $P(k)$ and k have both lower power law exponents and pre-factors. However, the pre-factor derived from each fault patch is variable along the fault scarps. Figure 8 illustrates this variability on the data acquired with the LiDAR on the Corona Heights fault, along the slip direction. A significant vertical shift is observed on the Fourier power spectra corresponding to the six different patches of the Corona Heights fault (Table 1b and Figure 8). The slopes, however, are similar (Table 1b and Figure 7). We emphasize that, for some patches this spatial variability on the pre-factor is clearly larger than the size of the error bars in the average spectral values (see Figure 8, for example between Corona-A and Corona-E). We suspect that this variability of roughness reflects the natural variability of an underlying stationary pre-factor distribution. This observation shows the difficulty to capture the overall mean value of the pre-factor of the surface roughness. Even if the Hurst exponent is similar for our LiDAR-scale patches, it is probable that they may reflect local variations in the pre-factor and extremely large sample may be required to capture the overall mean pre-factor value.

[30] One way to more easily interpret this log-log graph and to compare our results with previous studies like *Sagy et al.* [2007], is to convert the power spectrum module in term of root-mean square (*RMS*) roughness amplitude using Parseval's Theorem [*Brodsky et al.*, 2011]. Indeed if $0 < H_{\parallel,\perp} < 1$, for a profile of length L, the integration of $P(k) = C_{\parallel,\perp} k^{-1-2H_{\parallel,\perp}}$ over the wavelength λ (with $\lambda = 1/k$) yields that the *RMS* roughness correlates as $RMS = (C_{\parallel,\perp}/2H_{\parallel,\perp})^{0.5} L^{H_{\parallel,\perp}}$. In this sense, power law fits for three self-similar rough surfaces (*i.e.*, $H = 1$) with various pre-factors ($RMS = 0.1$ L, $RMS = 0.01$ L, $RMS = 0.001$ L) are shown on Figure 8 in order to compare our results with previous studies.

[31] In order to highlight the specific trend of each fault in the spectral domain, we have averaged the similar spectra (that means spectra with an approximately identical slope but with a slightly different vertical position) obtained from each scanner device. Each curve on Figure 9 therefore represents an average of similar spectra obtained for multiple fault patches. In this way, this technique gives a smoother spectrum that represents the global self-affine character of the entire

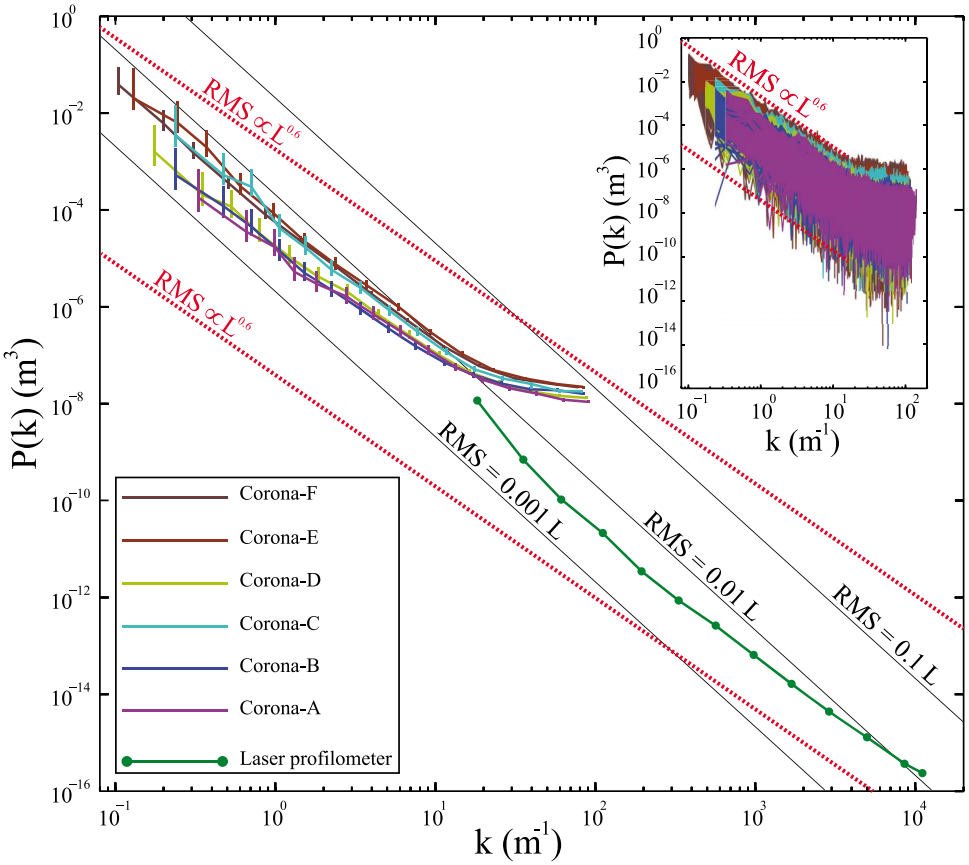

Figure 8. Illustration of the pre-factor variability along the Corona Heights fault. Log-log graph gathering the global laser profilometer spectrum with the 6 averaged LiDAR spectra. The inset shows all individual 2-D LiDAR spectra of each individual profiles extracted from the six fault patches. The same color code is respected for each averaged LiDAR spectrum and their respective 2-D LiDAR spectra. The intercept range of all 2-D LiDAR spectra is highlighted by the two dashed red power laws ($RMS \propto L^{0.6}$). The global laser profilometer spectrum falls in this range of intercepts sampled by the whole population of individual profiles that we explored at the LiDAR scale. Dark lines represent power law fits for three self-similar rough surfaces (*i.e.*, $H = 1$) with various pre-factors, that are: $RMS = 0.1$ L, $RMS = 0.01$ L, $RMS = 0.001$ L.

fault surface at the specific scales accessible by each device, while preserving good wavelength resolution. Each global spectrum has a similar slope, but in most cases it is difficult to connect them all together with a unique linear trend (Figure 9).

[32] The difficulty in connecting the scales is a direct consequence of the previously described spatial variability of the pre-factor along the fault surface (Figure 8). When we compute the scaling from the LiDAR measurements, we average all the 2-D power spectra of all individual rough profiles extracted from different fault patches (Figures 5 and 8). Each of these profiles has a different pre-factor but the average gives one specific pre-factor characterizing the global 3-D geometrical property of the fault surface at the LiDAR scale. At smaller wavelengths, with another device (i.e., laser profilometer or WLI), we select several sub-regions with one given average pre-factor among the whole population that we explored at larger scale (*i.e.* with the LiDAR) but not necessarily equal to the global pre-factor of the large scale measurements (see Figures 8 and 9). In other words, with the laser profilometer or the WLI, we expect to sample rougher or/and smoother sub-regions of the fault (i.e., with a pre-factor magnitude that is, respectively larger or smaller) than the global behavior recorded by the LiDAR by combining data over the full surface. As a consequence, it is clear that for the same fault, the specific global spectra calculated for each device by stacking similar spectra obtained for several fault patches, might be vertically shifted in some cases as observed in Figure 9. Finally, this variability in the pre-factor: (i) explains why the Hurst exponents have to be necessarily calculated separately for each device, and (ii) implies that it is not necessary to invoke a change in slope to connect the vertically shifted global spectra in Figure 9.

[33] To summarize, our analysis highlights that the roughness of the five fault scarps studied can be characterized over more than 5 decades of length scales (between 0.05 mm and 10 m) by one universal Hurst exponent in the direction of slip and a distinct one perpendicular to slip even if it is difficult to point out a single pre-factor in each direction. This description of the fault surfaces is independent of the geological context, i.e., lithology (rhyolite, chert, and limestone) and tectonic regime (strike-slip, oblique and normal). No clear relationship is observed in this particular data set between the range of

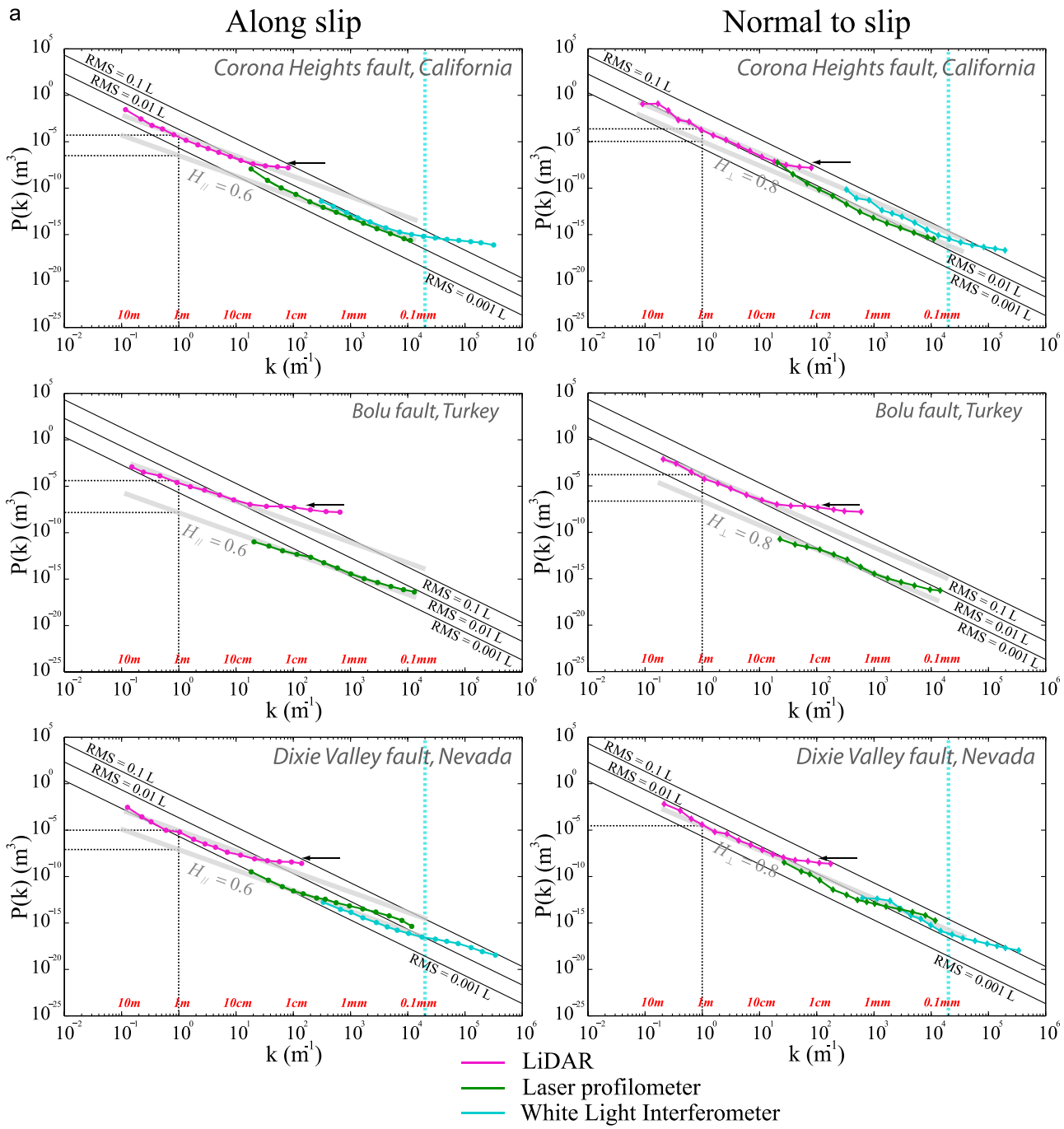

Figure 9. Combined Fourier power spectra from the five faults analyzed (left) along the slip direction and (right) perpendicular to it. Each curve at each scale (LiDAR, laser profilometer, white light interferometer) includes together the average spectrum of several sub-surfaces (or fault patches in Table 1b). Power law fits (thick gray lines) with a roughness exponent of $H_{\parallel} = 0.6$ and $H_{\perp} = 0.8$, connecting the field and laboratory data in both directions, are shown on plot for eye guidance. The black arrow and the vertical blue dashed line indicate, respectively: the level of noise of the LiDAR and the lower limit for the fit performed at the WLI scale. Dotted black lines indicate the range of pre-factors, $C_{\parallel,\perp}$, ($P(k) = C_{\parallel,\perp}\, k^{-1-2H_{\parallel,\perp}}$), extracted from the power law fits at $k = 1$ m (see all the values in Table 3), and used for Figure 10. Dark lines represent power law fits for three self-similar rough surfaces (*i.e.*, $H = 1$) with various pre-factors, that are: $RMS = 0.1$ L, $RMS = 0.01$ L, $RMS = 0.001$ L.

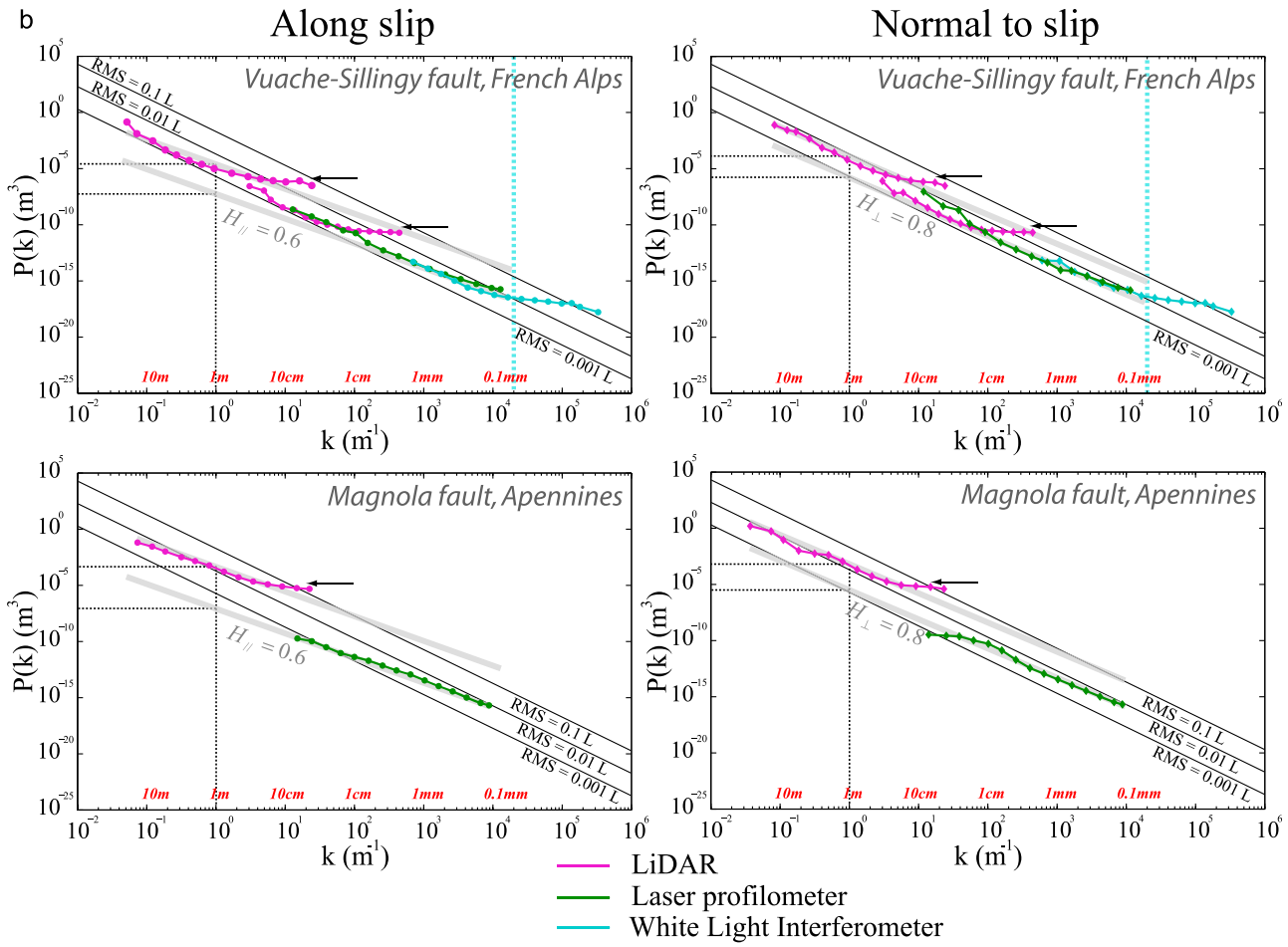

Figure 9. (continued)

pre-factor magnitude extracted from the global spectra shown in Figure 9 for each fault (see Table 3 for a complete list of the maximum and minimum pre-factors of each faults), and the slip estimated for the fault zone (see Figure 10).

4.2. Roughness of Large Continental Earthquakes Surface Ruptures

[34] In Figure 11, a compilation of the roughness results is provided for the thirteen surface ruptures. Results of the Fourier power spectrum analysis are shown for the individual segments (bounded by abrupt steps), and the whole rupture trace. For each surface rupture trace, each individual segment has a roughly identical self-affine exponent (see also Table 2) at large scales (i.e., above the regime controlled by data re-sampling – see Section 2.3). Moreover, the profiles obtained for the entire "reconstructed" rupture traces represent an average of the roughness over all the individual segments and keep an approximately identical self-affine exponent (Figure 11).

[35] A variability in the power spectrum amplitude (i.e., in the pre-factor) of the profiles extracted from the exhumed fault scarps (see Section 4.1) is also observed between each individual segment of the rupture traces. More precisely, along the rupture traces, individual segments display variability in the roughness amplitude but keep the same self-affine scaling properties of amplitude versus length scale (Figure 11), i.e., the same power law exponent. Since the 2-D roughness scaling properties of the reconstructed rupture traces correspond to a sum of those of the individual segments, it is to be expected that their spectra fall between those of the smoothest and the roughest short segments (Figure 11). In this way, the range of pre-factors inferred by the individual segments can be interpreted as a typical fluctuation in the estimated pre-factor of the "reconstructed" rupture traces.

[36] On the same log-log graph (Figure 12a), a stack of all the spectra calculated on the whole rupture traces, complements Figure 11 and emphasizes that all of the surface rupture data can be described by a single self-affine exponent of 0.8 ± 0.1. Another interesting result highlighted in Figure 12a is that, even though the thirteen rupture traces clearly sample variable geological settings, the same self-affine exponent fits all of the data. Interestingly, it is important to note here that the power spectral estimates of the thrust/normal ruptures traces are slightly higher than those of the strike-slip rupture traces. Finally, even though the surface rupture traces are related to fault zones which have accumulated a large range of finite geological slips (see Table 2), no trend is revealed between this parameter and the 2-D roughness scaling of the rupture traces. Indeed, taking into account both (i) the average pre-factor of each whole rupture traces and (ii) their respective typical fluctuations extracted from the corresponding individual

Table 3. Pre-factor (Exhumed Slip Surfaces)

	Pre-factor (m^3)	
Fault Name	Parallel to Slip	Perpendicular to Slip
Vuache-Sillingy		
Min	8×10^{-8}	2×10^{-6}
Max	2×10^{-5}	1×10^{-4}
Corona Heights		
Min	4×10^{-7}	1×10^{-5}
Max	5×10^{-5}	2×10^{-4}
Bolu		
Min	2×10^{-8}	3×10^{-7}
Max	5×10^{-5}	2×10^{-4}
Dixie Valley		
Min	1×10^{-7}	2×10^{-5}
Max	1×10^{-5}	
Magnola		
Min	1×10^{-7}	5×10^{-6}
Max	5×10^{-4}	8×10^{-4}

segments, no correlation appears with finite geological slip (Figure 12b).

5. Discussion

5.1. Can Surface Measurements of Faults Be Correlated With Earthquake Processes at Depth?

[37] First, we discuss how our measurements, performed on surface outcrops, could be relevant to faulting processes that occur at crustal depths up to 15 km. It is still debatable if the structural complexity of faults observed at the surface of the earth is preserved at depth. For example, some propose that the geometry of fault is more complicated at the surface than at depth [e.g., *Sylvester*, 1988], but the recent work of *Wei et al.* [2011] on the 2010 El Mayor-Cucapah earthquake shows that on the contrary faults are more irregular at depth than at the surface. *Schmittbuhl et al.* [2006] noted that outcrop roughness measured at the surface, i.e., under zero normal stress, can translate at depth into a simple fault geometry but strong normal stress fluctuations due to the elastic stresses at large confining pressures.

[38] On the five faults we have studied, two of them (Magnola and Dixie Valley) have a mainly normal component and their roughness has therefore recorded processes at work in the first kilometers of the crust. For the three other strike-slip faults, the roughness has recorded only shallow depth faulting processes. Dixie Valley and Bolu outcrops have recorded the surface termination of major earthquakes in the last century. For all faults, we find roughness exponents in the range 0.6–0.8. This can be compared to recent studies of the roughness of exhumed faults in the Sierra Nevada and Italian Alps [*Griffith et al.* 2010; *Bistacchi et al.*, 2011]. In these studies, the roughness of fault traces was characterized on outcrops for which the deep origin (c.a. Ten km depth) of the faulting process could be identified because of the presence of pseudotachylites and specific mineral assemblages. *Griffith et al.* [2010] indicated Hurst exponents

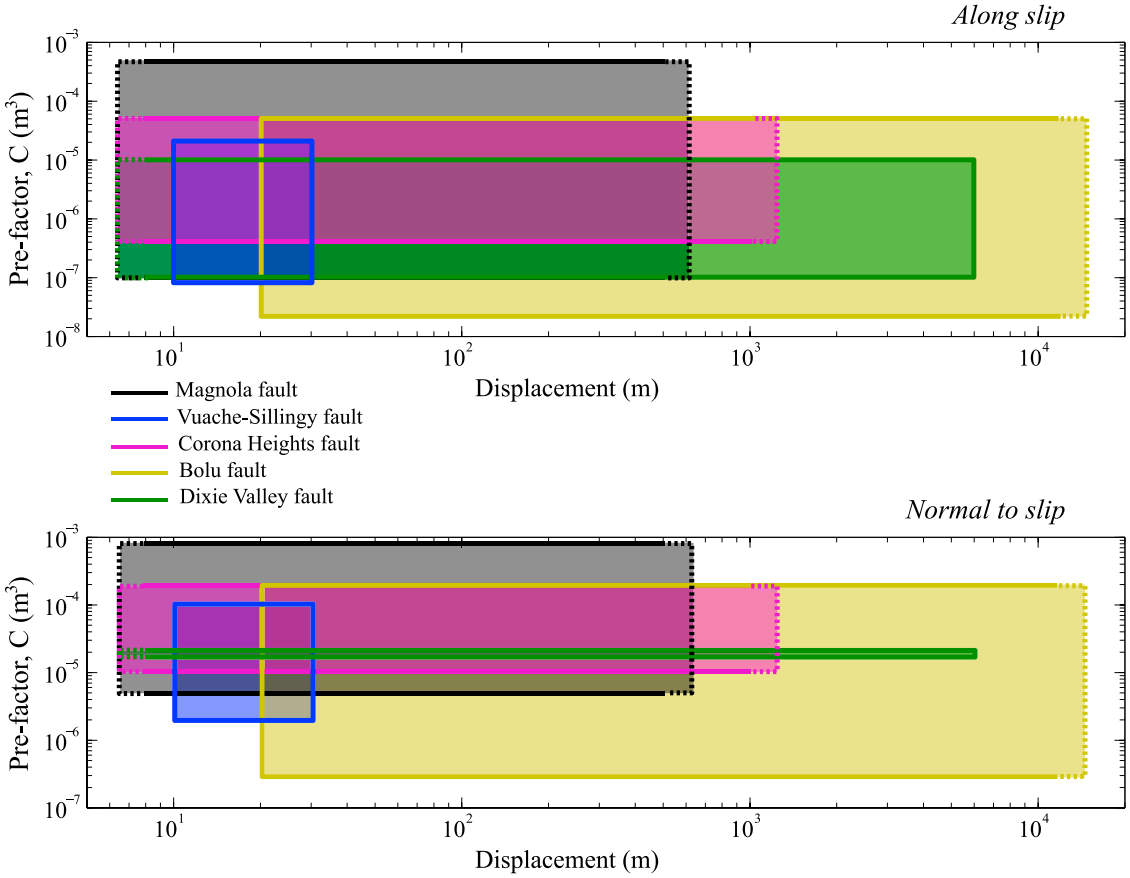

Figure 10. Log-log plots of the range of global pre-factor magnitude of the five faults extracted from Figure 9 (see also Table 3) versus the estimated slip (Table 1a).

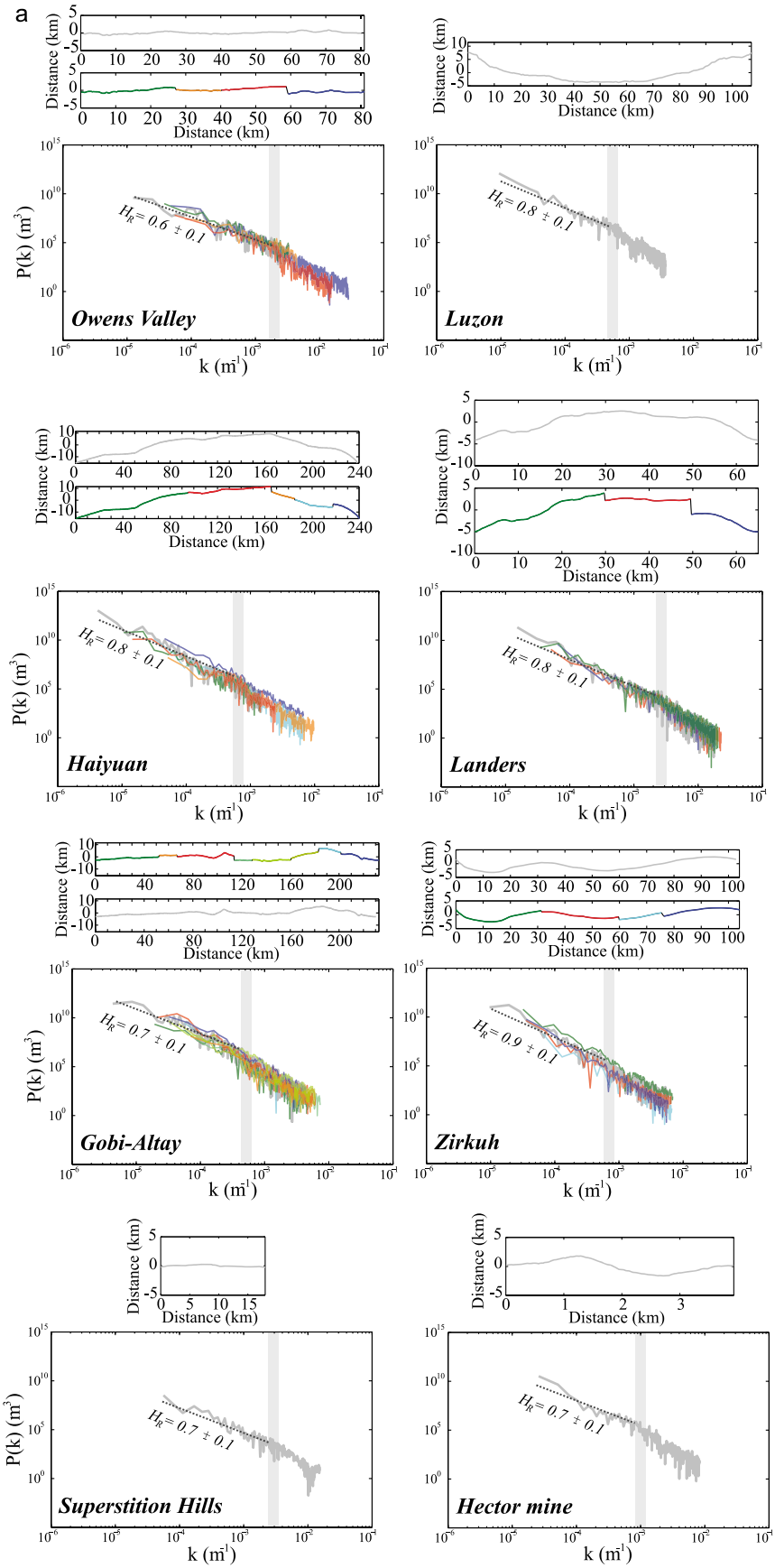
a
Distance (km)
P(k) (m³)
k (m⁻¹)
Owens Valley
$H_R = 0.6 \pm 0.1$
Luzon
$H_R = 0.8 \pm 0.1$
Haiyuan
$H_R = 0.8 \pm 0.1$
Landers
$H_R = 0.8 \pm 0.1$
Gobi-Altay
$H_R = 0.7 \pm 0.1$
Zirkuh
$H_R = 0.9 \pm 0.1$
Superstition Hills
$H_R = 0.7 \pm 0.1$
Hector mine
$H_R = 0.7 \pm 0.1$

Figure 11

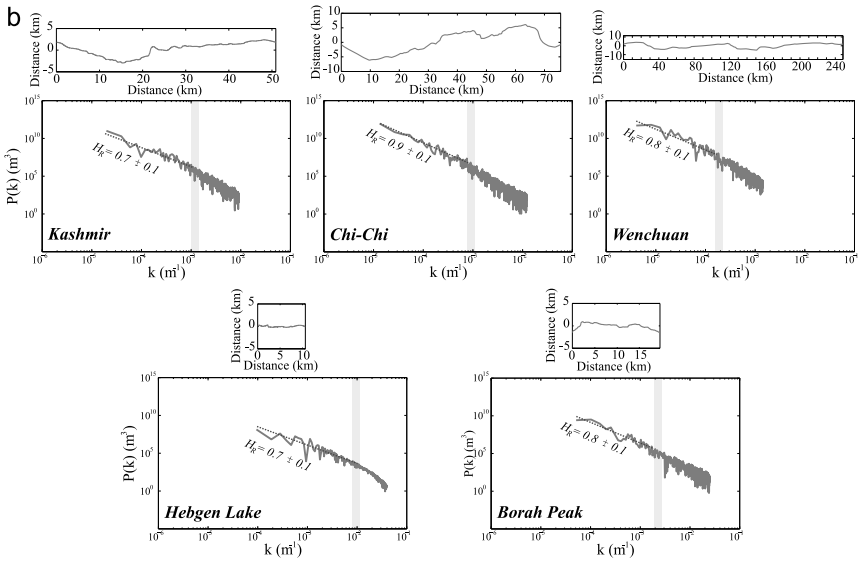

Figure 11. (continued)

with a quite large variability, in the range 0.4–1. Interestingly, *Bistacchi et al.* [2011] reported Hurst exponents in the range 0.6–0.8 for spatial scales in the range 0.5 mm–500 m, similar to those observed in our data and suggesting that the roughness property of faults is also maintained at depth. In the same way, high resolution 3-D reflection seismic data of *van Gent et al.* [2009] highlight that the large scale undulations of the fault plane observed at the surface are still preserved at depth.

5.2. Implications of the Self-Affine Scaling of the Fault Roughness on Earthquake Mechanics

[39] Based on the results of kinematic source inversion models that reconstitute the spatiotemporal evolution of slip during an earthquake, several studies show that both coseismic slip and stress appear to be very heterogeneous along the fault plane [*Bouchon*, 1997; *Mai and Beroza*, 2002]. A possible explanation is that the geometrical asperities of the fault plane concentrate stress and slip heterogeneities at various spatial scales. In this sense, based on self-affine geometrical description of fault surfaces as highlighted in our present work, recent numerical and theoretical studies have shown that the morphology of fault planes could control the dynamics of faulting and slip. Indeed, *Schmittbuhl et al.* [2006] have proposed that the initial heterogeneous stress distribution before an earthquake along the fault plane could reflect the elastic asperity squeeze of two self-affine fault planes. Their numerical solution is supported by the seismological inversion performed by *Bouchon* [1997] after the Kobe earthquake (M7, 1995) along the Nojima fault plane. *Candela et al.* [2011a], based on numerical modeling, have demonstrated that the heterogeneous coseismic spatial slip distribution could illustrate the relevance of the fault surface roughness. Their results are in agreement with the extended analysis of spatial correlations of slip maps for 44 earthquakes [*Mai and Beroza*, 2002]. Following a theoretical approach, *Candela et al.* [2011b] have derived the scaling evolution of stress-drop after an earthquake in relation to the self-affine properties of the fault roughness. Finally, *Dunham et al.* [2011] have shown that fault roughness is also a useful parameter that should be taken into account when calculating the expected seismic radiation.

[40] All these recent works directly linking the self-affine roughness of fault surfaces with the mechanics of earthquakes constitute promising studies. Using our realistic geometry of rough fault surfaces in seismic rupture dynamic models will surely provide new keys to move forward toward a better understanding of the fundamentals of earthquake behavior.

5.3. Reconciling the Roughness Properties of the Scanned Fault Surfaces and Rupture Traces

[41] Rupture traces are expected to be the spatial continuation of the fault surfaces to larger scales. Nevertheless, our analysis on geometrical properties of rupture traces (at scales of several hundred meters to ~50 km) do not reveal the anisotropic character of the roughness of the fault surfaces scanned. Indeed one might expect the anisotropy to be manifested as a difference between properties of strike-slip traces (which are nominally slip parallel) and dip-slip traces (which

Figure 11. Compilation of the surface rupture roughness results: (top) Digitized rupture traces and (bottom) corresponding Fourier power spectrum. Because of the abrupt steps biasing the Fourier transform computation, we have eventually performed this roughness analysis on each individual segment between two steps of the whole profile. The same color code is used for the individual segments and the corresponding spectra. In addition, the gray rupture profile and the corresponding gray Fourier power spectrum represent a reconstruction of the entire profile. Power law fits and the inferred Hurst exponents on the linear part of each curves at large scale (above the crossover length scale indicated by the gray vertical bar and marking the beginning of the regime controlled by data re-sampling) are represented on each graph.

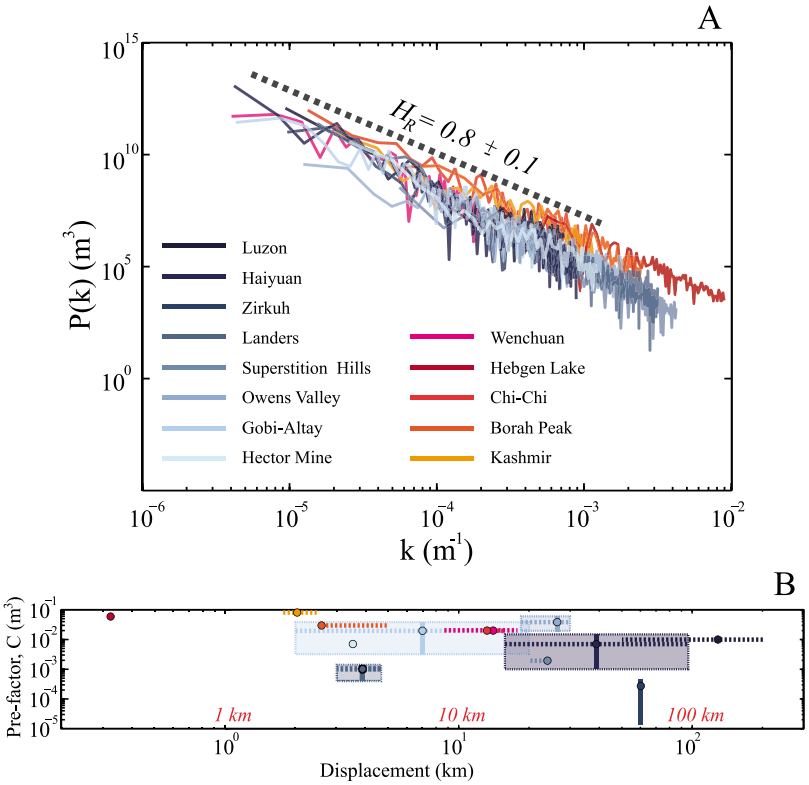

Figure 12. Variability of the pre-factor and slip accumulated for the thirteen studied rupture traces. (a) Stack of all the Fourier power spectra of the whole surface ruptures, underlining the global trend of the self-affine behavior at large scale. Power law fit with an average Hurst exponent of 0.8 ± 0.1 is indicated. (b) Log-log plot of the average pre-factors as a function of the finite geological slip for each rupture traces (see Table 2).

are nominally slip perpendicular). However, except for the slight higher pre-factor for the normal/thrust rupture traces compared to the strike-slip rupture traces, we do not observe a significant difference in their Hurst exponents (see Figures 11 and 12). In addition, the spatial correlations of the rupture traces are characterized by H_R = 0.8 ± 0.1 and pre-factors magnitudes close to those in the direction perpendicular to slip for the five scanned fault surfaces (Figure 13). Here, we suggest that this difference is due to the fact that the slip direction is not strictly sampled in the case of the natural rupture traces in contrast to the aligned profiles on the scanned fault surfaces.

[42] Several factors complicate sampling the roughness properties along one direction in the case of the rupture traces. First, a slight vertical component along the whole rupture trace of strike-slip faults is responsible for an oblique sampling with respect to the slip direction. Second, slip distributions of strike-slip earthquakes show that at some locations a vertical component of slip could be significant [*Florensov and Solonenko*, 1965; *Kurushin et al.*, 1997]. Indeed, the rupture traces show a structural complexity underlined by relay zones (compressive and extensive jogs), and bends, which could locally accommodate a significant vertical displacement at many locations along the fault [*Klinger et al.*, 2006]. In this case the rupture surface profile (or trace) morphology includes contributions from roughness along profiles parallel to the slip direction, and profiles perpendicular to the slip direction (but still in the fault plane). Third, the nonplanar ground surface topography that is present along the rupture trace also complicates the actual alignment of the sample profile. Even if the rupture event has pure horizontal or vertical motion, due to the roughness of the landscape topography, the geometrical properties of their surface traces should be always a combination of the along and normal slip roughness. Each of these three factors results in traces that contain a mixture of the slip-parallel and slip-perpendicular roughness. We can therefore generalize our discussion by considering the overall effects of mixing slip-parallel and slip-perpendicular components.

[43] In Figure 14, we investigate this mixing effect on the estimated Hurst exponents and pre-factors into two complementary ways. Figure 14a presents the effect of sampling a profile oblique to the slip direction. This test is devoted to estimate the effect of a slight vertical slip-component along the whole strike-slip rupture traces. The Hurst exponents and the pre-factors of a synthetic anisotropic self-affine surface (see Appendix A1), computed using a Fourier based method [*Candela et al.*, 2009], and with a roughness root-mean square standard deviation that scales as $RMS = 0.005\ L^{0.6}$ in slip direction and $RMS = 0.015\ L^{0.8}$ normal to it, were calculated on series of 2-D profiles extracted at an angle θ from the slip direction. The same procedure was performed on a scanned patch of the Corona Heights fault (Corona-A in Table 1b). A clear similarity is observed in the angular variability of the roughness exponent and the pre-factor computed for the synthetic surface and the natural fault patch (considered as representative of our set of fault surfaces). Both surfaces expose the same nonlinear dependence of the

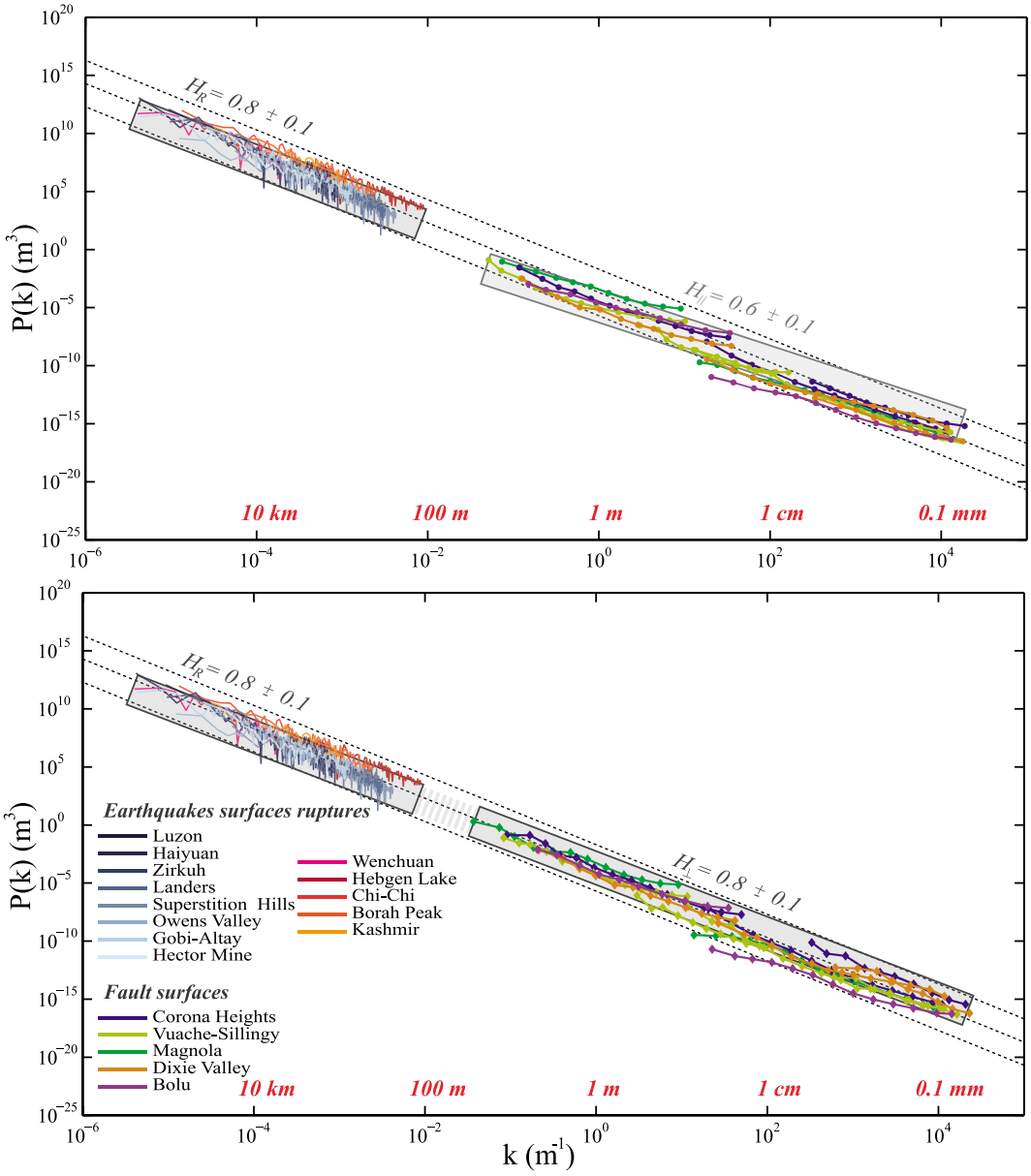

Figure 13. Comparison of the roughness of the earthquakes surface ruptures with that of the exhumed fault surfaces. The global spectra of the exhumed fault surfaces for the (top) along and (bottom) normal slip direction are plotted on a log-log graph together with those obtained for the thirteen continental earthquakes surface rupture traces. The exhumed fault data are identical to those plotted on Figure 9, and those of the surface ruptures correspond to that of Figure 12. Power law fits with a Hurst exponent of 0.8 and 0.6 are shown (gray lines). For the sake of comparison with previous studies, power law fits for three self-similar rough surfaces (*i.e.*, $H = 1$) with various pre-factors ($RMS = 0.1$ L, $RMS = 0.01$ L, and $RMS = 0.001$ L), are displayed (dashed dark lines).

Hurst exponent with the azimuthal direction of profile extraction (θ), as pointed by *Renard et al.* [2006] and *Candela et al.* [2009] using different statistical tools. When departing a few degrees from the direction of the smallest exponent, i.e., the slip direction, the Hurst exponent sampled is already very close to the largest exponent, *i.e.* the direction normal to slip. In contrast, the pre-factor linearly evolves with θ. In Figure 14b, we estimate the Hurst exponents and the pre-factors of composite synthetic profiles formed by the association of two profiles with a roughness root-mean square standard deviation that scales respectively as $RMS = 0.005\ L^{0.6}$ and $RMS = 0.015\ L^{0.8}$. In this way, the effect of sampling a combination of slip-parallel and slip-perpendicular topography along the rupture trace is reproduced, as it could be the case due to the landscape topography and/or some local vertical slip. As observed previously, the Hurst exponent and the pre-factor increase respectively nonlinearly and linearly with the increase of the percentage of the composite profile scaling as $RMS = 0.015\ L^{0.8}$.

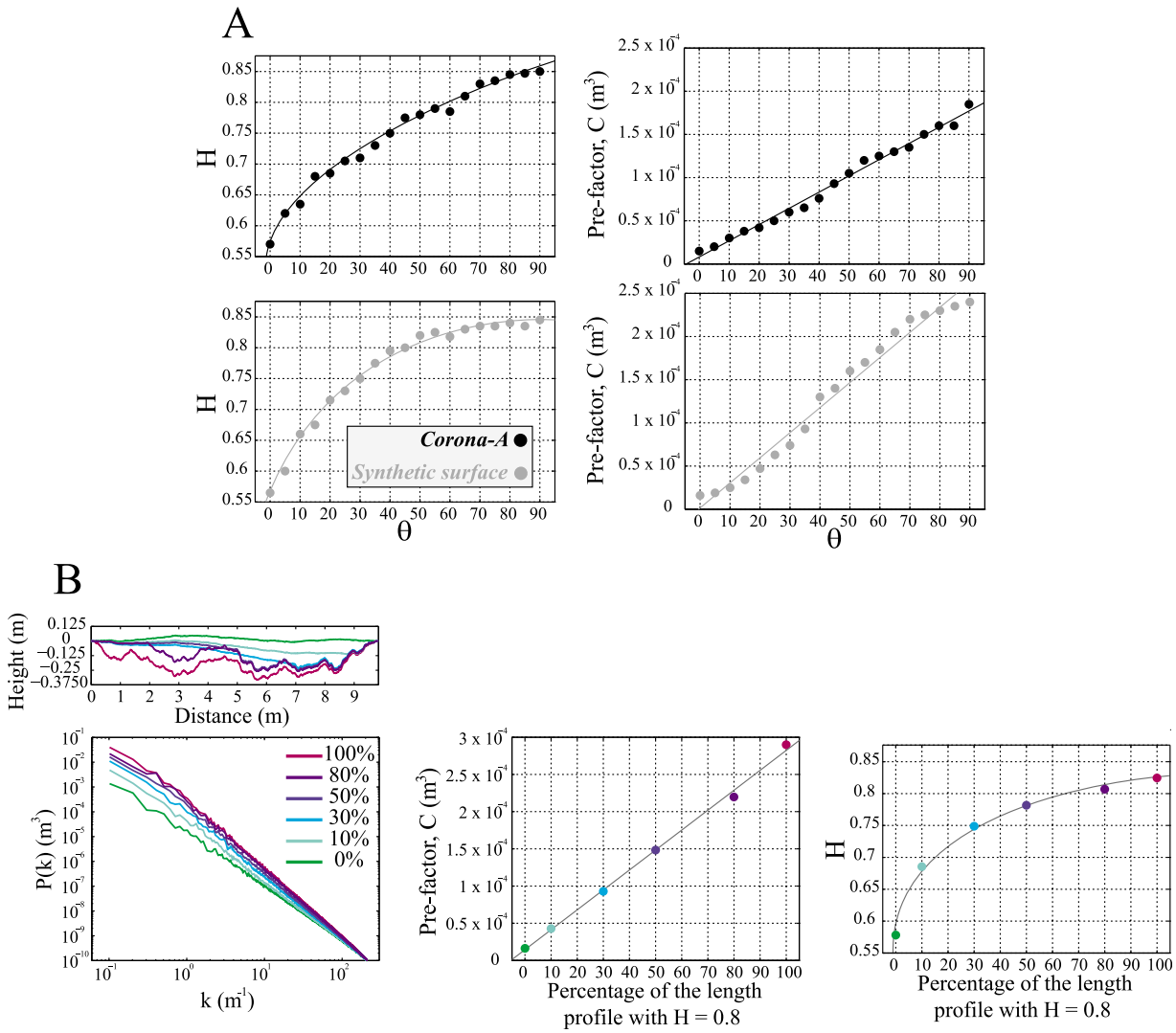

Figure 14. Mixing effect on the roughness properties. (a) Angular dependence of the Hurst exponent (left) and the pre-factor (right) computed on a synthetic anisotropic self-affine surface with two input exponents in perpendicular directions ($H_{\parallel}$ = 0.6 and $H_{\perp}$ = 0.8), and for a patch (Corona-A, see Table 1b) scanned with the LiDAR. The Hurst exponents and the pre-factors were calculated on series of 2-D profiles extracted at an angle θ between the slip direction (θ = 0) and the perpendicular direction (θ = 90). (b) (left) Fourier spectrum of synthetic profiles composed by the association of two profiles with a roughness root-mean square standard deviation that scales respectively as $RMS = 0.005\ L^{0.6}$ and $RMS = 0.015\ L^{0.8}$. Starting with a profile scaling as $RMS = 0.005\ L^{0.6}$, we estimate here the dependence of the Hurst exponents (middle) and the pre-factors (right) with the increase of the percentage of the profile scaling as $RMS = 0.015\ L^{0.8}$.

[44] These two tests independently highlight the nonlinear and linear increase of the Hurst exponent and the pre-factor, respectively, as a function of the fraction of slip-parallel topography mixed with slip-perpendicular topography. Consequently, a small degree of mixing could explain why the roughness of the strike-slip rupture traces is characterized by a Hurst exponent already close to the normal slip value of the scanned fault surfaces. In contrast to the Hurst exponent, the linear response of the pre-factor implies that for example a strong vertical component of slip along the whole strike-slip rupture traces is necessary to produce pre-factors magnitudes close to the normal slip value of the scanned fault surfaces. However, it is probable that the coupling of the two effects, independently dealt in Figure 14, could explain the large pre-factors of the strike-slip rupture. In other words, a slight vertical slip-component along the whole strike-slip rupture traces (dealt in Figure 14a) coupled with the effect of the landscape topography and some local vertical slip (dealt in Figure 14b), could explain why their pre-factors are close to that of the range of the normal slip direction. Interestingly, the respective nonlinear and linear increase of the Hurst exponent and the pre-factor relatively to an increase of the mixing of a slip-parallel topography with a slip-perpendicular topography are in agreement: (i) with the slight lower pre-factor of the

strike-slip rupture traces compared to the normal/thrust traces and (ii) with the fact that no significant difference in their Hurst exponents is observed (see Figure 12).

[45] The data therefore suggest that the self-affine regime observed at the outcrop scale is also present at the map-scale of earthquake rupture traces. Even though there is a gap in the data between scanned fault surfaces and rupture traces (that remains to be investigated), and that traces do not directly constrain only the slip-parallel geometry, a single self-affine geometrical description fits our measurements from the microscopic (WLI) scale to the map-scale of rupture traces (see Figure 13). As already mentioned, analyzing the roughness of the Gole Larghe fault zone (Italian Alps), *Bistacchi et al.* [2011] have recently reported Hurst exponents in the range 0.6–0.8 for spatial scales in the range 0.5 mm–500 m and therefore bridging the gap of our data.

5.4. Pre-factor Variability and Displacement

[46] In Section 4.1, we found no significant relationship between the roughness amplitude (i.e., the pre-factor magnitude) and the cumulative slip estimated for the scanned fault surfaces (Figure 10). Other recent studies [*Sagy et al.*, 2007; *Mitchell and Faulkner*, 2009; *Savage and Brodsky*, 2011] have noticed changes in fault roughness and damage parameters as a function of slip for faults spanning a range of displacements shifted from the data set here. For example, *Sagy et al.* [2007] noticed a difference for faults that have slip larger than approximately 10 m versus those that have slip lower than 1 m. Our data set contains faults with displacements larger than several meters (Table 1a) which is within the large-slip fault population. Accordingly our results are consistent with these previous observations. In addition, even if we focus on the smoothest sub-surfaces of each fault (i.e., the lower bound of the range of pre-factors), no correlation is revealed with the estimated slip accommodated (see Figure 10). The lack of a discernible evolution signal in our limited data set is also consistent with the wide range of displacement data of *Brodsky et al.* [2011] that also shows that smoothing is a very weak process once >10 m of slip is accumulated.

[47] Another important result of our roughness scaling analysis is that no correlation was observed between the finite displacement of the fault zone hosting the rupture trace and its roughness (see Section 4.2 and Figure 12b). Note here that even if the standard deviation in our data is quite large and could hide the physical correlation, this observation is consistent with the study of *Klinger* [2010], who showed that correlation between characteristic fault segment length and thickness of the seismogenic crust is maintained, independently of the slip accumulated. In addition, we suggest in the present study that a consistent spatial organization persists over the entire range of accessible length scales (i.e., from several hundred meters to ~50 km), independently of the total geological slip. Note here that, following *Klinger* [2010], a specific length scale should appear at approximately 20 km, i.e., the thickness of the seismogenic crust. However, because of the lack of sufficient wavelength content between 20 km and 50 km, this probable characteristic length scale is not clearly revealed by our analysis.

[48] Smoothing of fault geometry has been suggested in other studies [*Wesnousky*, 1988; *Manighetti et al.*, 2007], and is thought to result from surface roughness of faults being inversely related to their total displacement. Such smoothing of a fault trace has primarily been studied by examining large scale geometrical asperities, such as step-overs of several kilometers. In our study, given that we remove these first-order geometric discontinuities to perform the Fourier transform analyses; we lose these fingerprints of the fault maturity.

[49] The notion of "geometric regularization" or "maturity" refers to the intuitive idea that the fault zone geometry becomes more and more flat during the successive slips by abandoning or smoothing the complexity of the initial structures (segments). *Ben-Zion and Sammis* [2003] recommended that it is necessary to separate the abandoned structural units from those which actively participate in the accommodation of the slip to reveal a possible regularization of the geometry of the fault zone with slip. It is therefore important to emphasize that both fault scarps scanned on the field and rupture traces are markers of the morphology of the active structures of fault zones. Our results thus demonstrate that the active portions of faults from the spatial scales of micrometer up to at least the thickness of the seismogenic crust preserve a complex geometry during successive displacements. In other words, the complexity of an active fault surface is spatially organized following a self-affine geometrical description, independently of the lithology and the tectonic regime. Our observations, like those of *Brodsky et al.* [2011], *Savage and Brodsky* [2011], and *Klinger* [2010], suggest that a re-roughening mechanism is active in the fault zone to maintain the geometrical complexity during successive slips. For example, as proposed by *Klinger* [2010], rupture might naturally branch on preexisting secondary faults as a result of the dynamic stress build-up ahead of the rupture [*Poliakov et al.*, 2002; *Bhat et al.*, 2004]. This effect could explain the persistence of some level of complexity and prevent the complete smoothing of the fault geometry. Moreover, as proposed by *Brodsky et al.* [2011], the lack of discernible evolution of roughness could be also explained by lubrication by the accumulated gouge that mitigates the abrasional smoothing that occurs during slip.

5.5. Scale-Free Process at the Origin of Fault Roughness

[50] Previous studies on natural fault surfaces [*Brown and Scholz*, 1985; *Power et al.*, 1987; *Power and Tullis*, 1991; *Lee and Bruhn*, 1996] have proposed that the slope of the Fourier spectrum could change from large to small scales, implying that different processes may be involved during the generation of surface fault textures at different spatial scales. In fact, any inflexion of the spectrum could correspond to a characteristic scale. Such a characteristic scale could be interpreted as the transition between physical processes. For example, *Lee and Bruhn* [1996] observed several characteristic length scales between 1 mm and several meters and attributed them to a combination of frictional ploughing, secondary fracturing, and intersections between anastomosing fractures along sliding surfaces. In the present study, a systematic bending of the Fourier power spectra (along both the parallel and the perpendicular slip directions) at the length scale 0.05 mm is observed on the WLI data (Figures 6 and 9). This change of regime occurs at larger length scales relative to the expected WLI resolution, and we suspect that it could be the hallmark of the transition between two

physical processes appearing at the grain scale. *Chen and Spetzler* [1993] suggest that a characteristic length scale appearing at the grain scale is due to a change in the dominant mode of deformation from small scale intergranular cracking to intragranular cracking at large scale. *Méheust* [2002] made the same observation and interpretation on tensile cracks at the grain scale. *Sagy et al.* [2007] also suggested a change in roughness at the sub-centimeter scale for large-slip faults. However, it was beyond the scope of this work to quantitatively characterize this possible characteristic length scale and we limited our scaling analysis to scales larger than 0.05 mm. Indeed, considering the variability of the pre-factor (see Section 4.1), we have demonstrated that an anisotropic mono-affine geometric description characterized by two different global Hurst exponents $H_{\parallel}$ = 0.6 and $H_{\perp}$ = 0.8 best fits the data between 10 m and 0.05 mm. In our data, acquired with three different devices spanning complementary scales and in agreement with *Schmittbuhl et al.* [1993], no variation of the Hurst exponent within the confidence limits is detected between 10 m and 0.05 mm. This observation could be evidence that a single, scale-free process control the roughness of the fault surfaces.

[51] Since the 1990s, increasing experimental evidence showed that the roughness exponent for mode I fractures surfaces had a universal value of about 0.80 [*Bouchaud et al.*, 1990; *Bouchaud*, 1997]. Simultaneously with these experiments, theoretical and numerical works have attempted to identify the origin of the self-affine scaling of fracture roughness [*Bouchaud*, 1997, *Alava et al.*, 2006; *Hansen and Schmittbuhl*, 2003; *Bonamy and Bouchaud*, 2011]. The common denominator of all this work is to model fracture propagation as a network of elastic beams, bonds, or electrical fuses with random failure thresholds. In other words, in order to reproduce the self-affine roughness exponent experimentally observed, the fracture propagation is assimilated as a damage coalescence process in a heterogeneous material. The localization and the roughness of the resulting fracture are therefore controlled by the long-range elastic interactions related to the multiscale coalescence of cracks.

[52] The fault zones studied here show a similar damaged structure characterized by a network of more or less developed anastomosing sliding surfaces that individualize lenses of damaged material (Figure 2). Such lenses have been described in various tectonic regimes from the seismic scale [*Gibbs*, 1983, 1984] down to the millimeter scale [*Gabrielsen and Clausen*, 2001; *Clausen et al.*, 2003; *Berg*, 2004; *Christensen*, 2004]. We propose here that elastic interactions related to linkage of many discrete slip surfaces, controlling the generation of the multiscale bumpy lenses observed on the scanned fault outcrops (Figure 2), could be the scale-free process at the origin of fault roughness. Indeed, even if shear cracks involve significantly higher energy release rates than tensile cracks [*Atkinson*, 1991], some similarities in the elastic influences on the stress field at the crack tip can be obtained theoretically [*Gao and Rice*, 1986; *Gao et al.*, 1991; *Atkinson*, 1991; *Schmittbuhl et al.*, 2003].

[53] Even if a single self-affine regime is maintained for the map-scale rupture traces, it remains difficult to support the fact that earthquake rupture roughness is also controlled by the same processes at work at the outcrop scale. However, it is noteworthy that the rupture traces may also be formed by multiscale segments [see, e.g., *Klinger*, 2010, Figure 5] whose growth and coalescence could be also controlled by long range elastic interactions.

6. Conclusion

[54] Using three independent scanner devices (a Light Detection And Ranging apparatus – also called LiDAR, a laser profilometer, and a white light interferometer), we have shown that the roughness of fault surfaces, spanning different geological contexts, can be characterized by a single anisotropic self-affine description with two Hurst exponents (one in the slip direction, $H_{\parallel}$ = 0.6 and one normal to the slip direction, $H_{\perp}$ = 0.8) from 0.05 mm scale to 10 m. Map-scale traces of thirteen earthquake ruptures show a behavior similar to the slip perpendicular measurements. Our analysis suggests that, even if the along or normal slip direction are not strictly sampled in the case of the rupture traces, a single geometrical description can be maintained over nine decade of length scales (between 0.05 mm and at least the thickness of the seismogenic crust, i.e., ~20 km). In addition, although the lack of data between the scanned fault surfaces and the rupture traces leaves a zone that remains to be investigated, recent works of *Bistacchi et al.* [2011] bridging the length scale gap appear to support our interpretation. Finally, it appears that once a small amount of slip has been achieved, the geometric complexity of the fault surfaces is maintained regardless of the amount of further slip accommodated. Consequently, we propose that processes that create this roughness and processes that destroy it must reach a dynamic equilibrium.

Appendix A: Potential Bias in Roughness Data

A1. Effect of the Noise of the Acquisition System

A1.1. Laboratory Scale

[55] The home-made laser profilometer and the WLI noise levels are well below the signal recovered from the fault surfaces (see Figure 6). A detailed description of the conditions under which measurements with this scanner device departs from the reality is given by *Méheust* [2002]. In addition, the slope of the spectra computed on WLI scans at spatial scales larger than 0.05 mm are consistent with those of laser profilometry for the same range of length scales (see Figure 9).

A1.2. Field Scale

[56] LiDAR data have the largest bias, we therefore focus our noise analysis on this instrument. Consequently, the results provided by the following analyses are considered as end-members of the noise estimate for the three instruments used in our study.

[57] In the spirit of the work of *Schmittbuhl et al.* [1995b] on the reliability of a self-affine measurement on 2-D rough profile, *Candela et al.* [2009] reviewed different statistical methodologies which allow the assessment and characterization of the anisotropic self-affine behavior of fault topography. That work was mainly devoted to precisely defining the intrinsic error of the statistical methods, such as the Fourier power spectrum, in estimating the scaling properties of fault surface roughness.

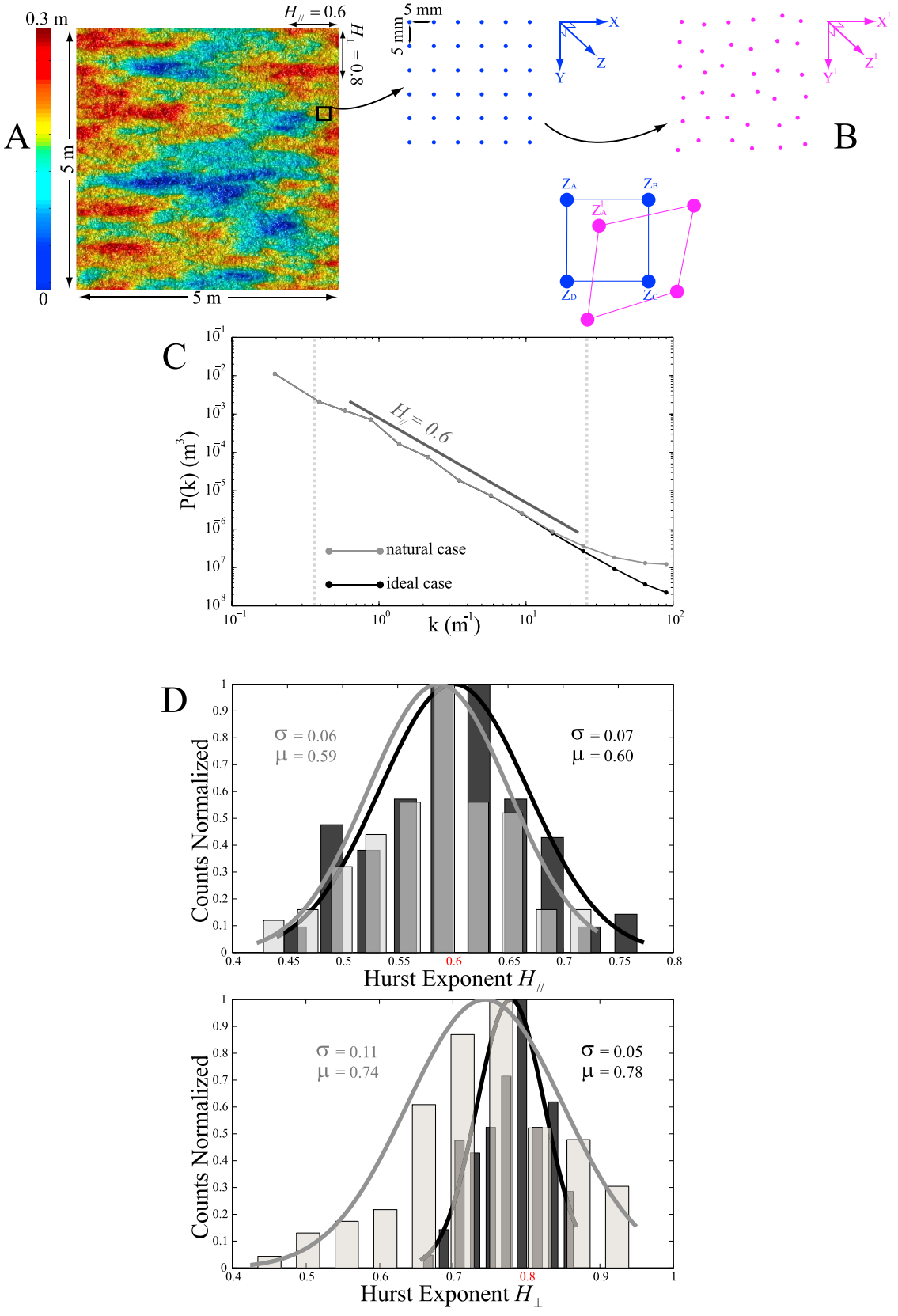
A
0.3 m
0
5 m
5 m
$H_{//} = 0.6$
$H_{\perp} = 0.8$
5 mm
5 mm
X
Z
Y
B
X^1
Z^1
Y^1
Z_A
Z_B
Z_A^1
Z_D
Z_C
C
P(k) (m^3)
k (m^{-1})
$H_{//} = 0.6$
natural case
ideal case
D
Counts Normalized
σ = 0.06
μ = 0.59
σ = 0.07
μ = 0.60
Hurst Exponent $H_{//}$
σ = 0.11
μ = 0.74
σ = 0.05
μ = 0.78
Hurst Exponent $H_{\perp}$

Figure A1

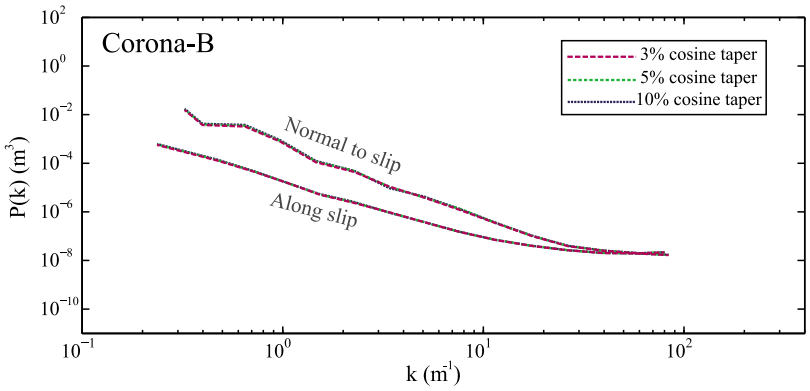

Figure A2. Effect of the taper function on the power spectral estimates. Log-log graph gathering the average spectra of one LiDAR fault patch (Corona-B, see Table 1b) computed with using in our process a taper function of 3%, 5%, and 10%.

[58] Here, a new test is performed by taking into account the error encountered in the spatial position (X, Y, Z) of each points measured by the 3-D laser scanner. We use a synthetic anisotropic self-affine surface [*Candela et al.*, 2009] of 5 × 5 m with an original regular point spacing of 5 mm (Figure A1), and with two different Hurst exponents in perpendicular direction ($H_{\|} = 0.6$ and $H_{\perp} = 0.8$). In order to simulate the error inherent to LiDAR data acquisition on the spatial position of each points (X, Y, Z), we add Gaussian white noise with a distribution of [0, 2.5 mm] on the original position of each point, to obtain the perturbed grid (X^1, Y^1, Z). Then the height Z^1 of each point at these new positions (X^1, Y^1) is computed by interpolating (bilinear interpolation) the four nearest points of each of these new positions on the original ideal model (Figure A1). In a final step, Gaussian white noise, with a standard deviation equal to 5 mm, is added on the interpolated heights Z^1, to yield the error of the LiDAR data in the vertical position.

[59] After generating this noisy cloud of points (X^1, Y^1, Z^1), we extract profiles oriented along the slip parallel and perpendicular directions as is done for the measurements, and estimate both Hurst exponents. The results are then averaged over 100 realizations of the synthetic surfaces. Due to the added noise, the Fourier power spectra flattens at short length scales (as for example in the slip direction shown in Figure A1), which results in a slight underestimation of the Hurst exponents. For both directions, along slip and perpendicular to it, we find that the median estimates of $H_{\|}$ and $H_{\perp}$ of the biased synthetic surfaces are 0.59 ± 0.06 and 0.74 ± 0.11 respectively, compared to the noise-free data where the Hurst exponents were 0.6 ± 0.07 and 0.78 ± 0.05, respectively. Note that the error bar of the estimated Hurst exponent of the biased synthetic surfaces is approximately twice larger in the direction perpendicular to slip relative to that in the slip direction. In both directions, even if the Hurst exponent is slightly underestimated for the noisy data, its value is still included in the range given by the standard deviation of the noise-free data.

A2. Effect of the Taper Function

[60] One other inherent difficulty in estimating the scaling properties of a rough profile by a Fourier analysis is how to remove the drift in the signal. In our procedure, as detailed in Section 3, when we reference heights to a line which passes through the first and last points of each individual profile, we effectively reposition the first and last points to the same height. Moreover, in order to ensure that there are no step functions at the end of each profile, we apply a cosine taper. This process is especially designed to minimize leakage. Figure A2 shows that in our data, due to the flatness of the roughness profiles, using a taper function of 3%, 5% or 10% does not modify significantly the power spectral estimates and therefore the final estimates of the Hurst exponent and the pre-factor. In our analysis, a taper function of 3% has been finally applied in order to preserve the original signal as much as possible. A detrending procedure using a best fit slope and a taper function also yields the same results.

A3. Effect of Re-sampling

[61] For each earthquake, once the surface rupture map has been digitized, the data set is re-sampled to a regular spacing to ensure consistent spatial sampling, independent of the length of each rupture. This re-sampling is performed to avoid bias due to local wiggles of the rupture trace (Klinger, 2010). We investigate here how this re-sampling process affects the spectra of the Fourier transform. The original digitized rupture

Figure A1. Effect of noise inherent to LiDAR data acquisition. (a) Ideal synthetic 5 × 5 m self-affine surface with an original regular point spacing of 5 mm. (b) Illustration of the addition of a noise in the regularly spaced original grid (X, Y, Z). (c) Comparison of the Fourier power spectra in direction of slip obtained for the ideal synthetic surface and the noisy synthetic surface. Both vertical dashed gray lines indicate limits taken for fitting the Hurst exponent. (d) Distribution of measured Hurst exponents, on 100 simulations, for the direction of slip and perpendicular to it. Black bars show the ideal simulated fault surface models, and the gray bars correspond to the noisy simulated fault surface models. The solid lines (black for the ideal case and gray for the natural case) represent the fits of the measurements to a normal distribution with mean μ and standard deviation σ given at the top left for the noisy natural case and the top right for the noise-free case.

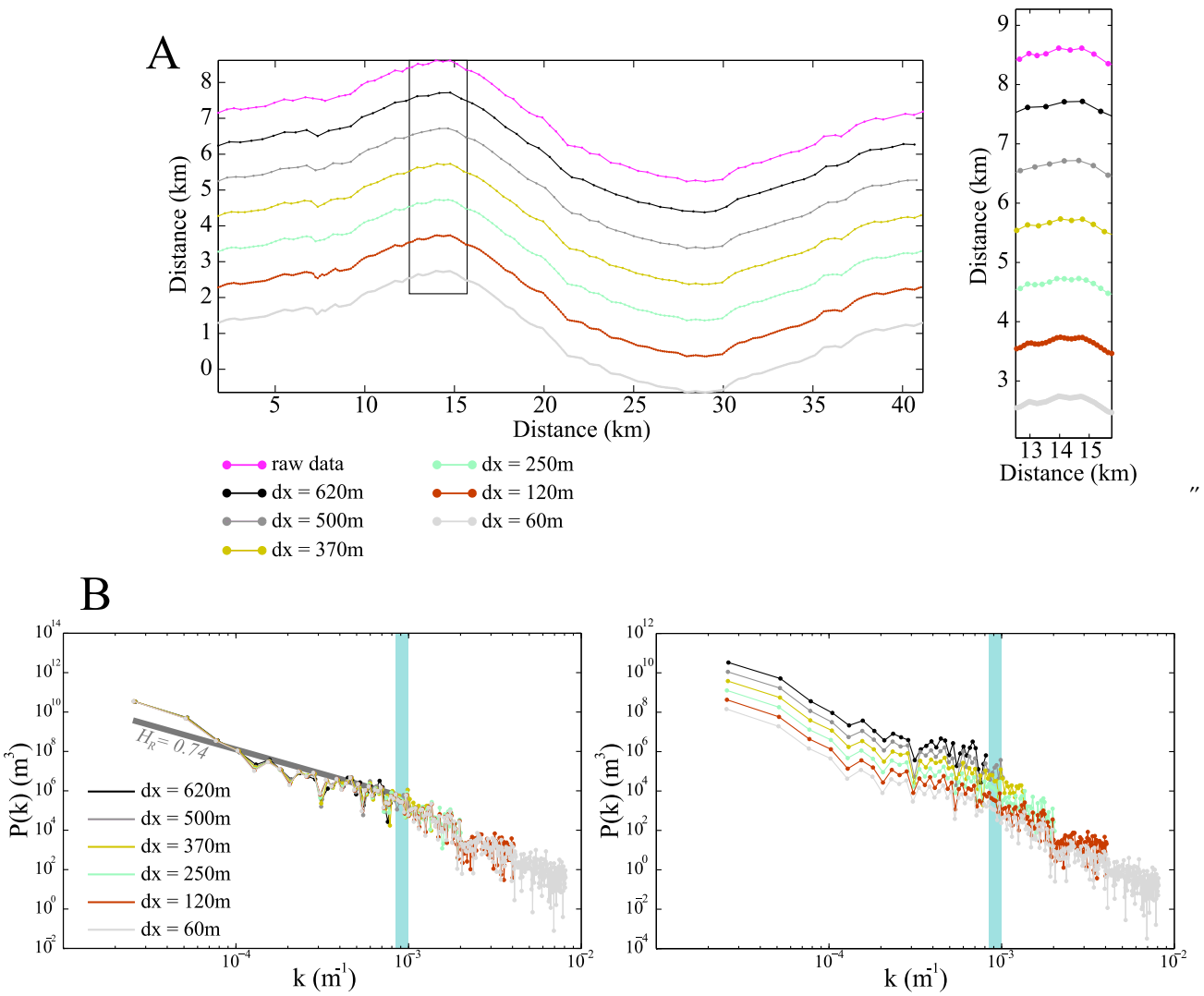

Figure A3. Effect of re-sampling on earthquake surface rupture roughness: example of Hector Mine earthquake. (a) Digitized surface rupture traces of the Hector Mine earthquake. The original rupture map with an irregular point spacing (pink profile) is re-sampled in order to ensure consistent spatial sampling with a regular spacing (δx). The inset indicates the position of the zoom located on the right, showing the irregular point spacing on the top and the gradual increase of the re-sampling (or decreasing of δx) with a regular point spacing of profiles downward. (b) Fourier power spectra of the digitized rupture traces shown in Figure A3a. Spectra colors are the same as in Figure A3a. On the right the spectra have been shifted vertically to improve the visibility. The blue vertical bar on both graphs highlights the crossover length scale, at approximately 1200 m, between both regimes: the lower regime is attributed to data re-sampling, the upper regime characterizes roughness properties of the digitized profiles with a Hurst exponent HR = 0.74.

trace of the Hector mine earthquake, taken as an example, is re-sampled with various constant values of δx in the range 60–620 m (Figure A3). In the Fourier power spectra of this set of digitized rupture traces, two regimes can be observed. At small scales, *i. e.* large wave numbers, (between approximately 120 m and 1200 m) the behavior can be attributed to data re-sampling. At large scales, *i.e.* small wave numbers (above 1200 m), a power law giving a Hurst exponent $H_R = 0.74$ represents the best fit. The crossover length scale between the two regimes corresponds to the maximum spacing between two points in the original data. Whatever the value of δx taken for re-sampling the data, the crossover length scale remains at the same position. We propose that the regime at large scales, characterizing roughness properties of the digitized ruptures traces is therefore not affected by data re-sampling; both the slope and the pre-factor of each spectrum are identical (Figure A3).

[62] The same re-sampling procedure has been performed on ideal synthetic self-affine profiles in order to precisely define if the scaling property could be modified (Figure A4). An original self-affine profile ($RMS = 0.01\ L^{0.6}$) with regular spacing of 500 m and a total length of 100 km (extracted from a synthetic surface as previously presented), is modified by adding to the X coordinates a Gaussian white noise

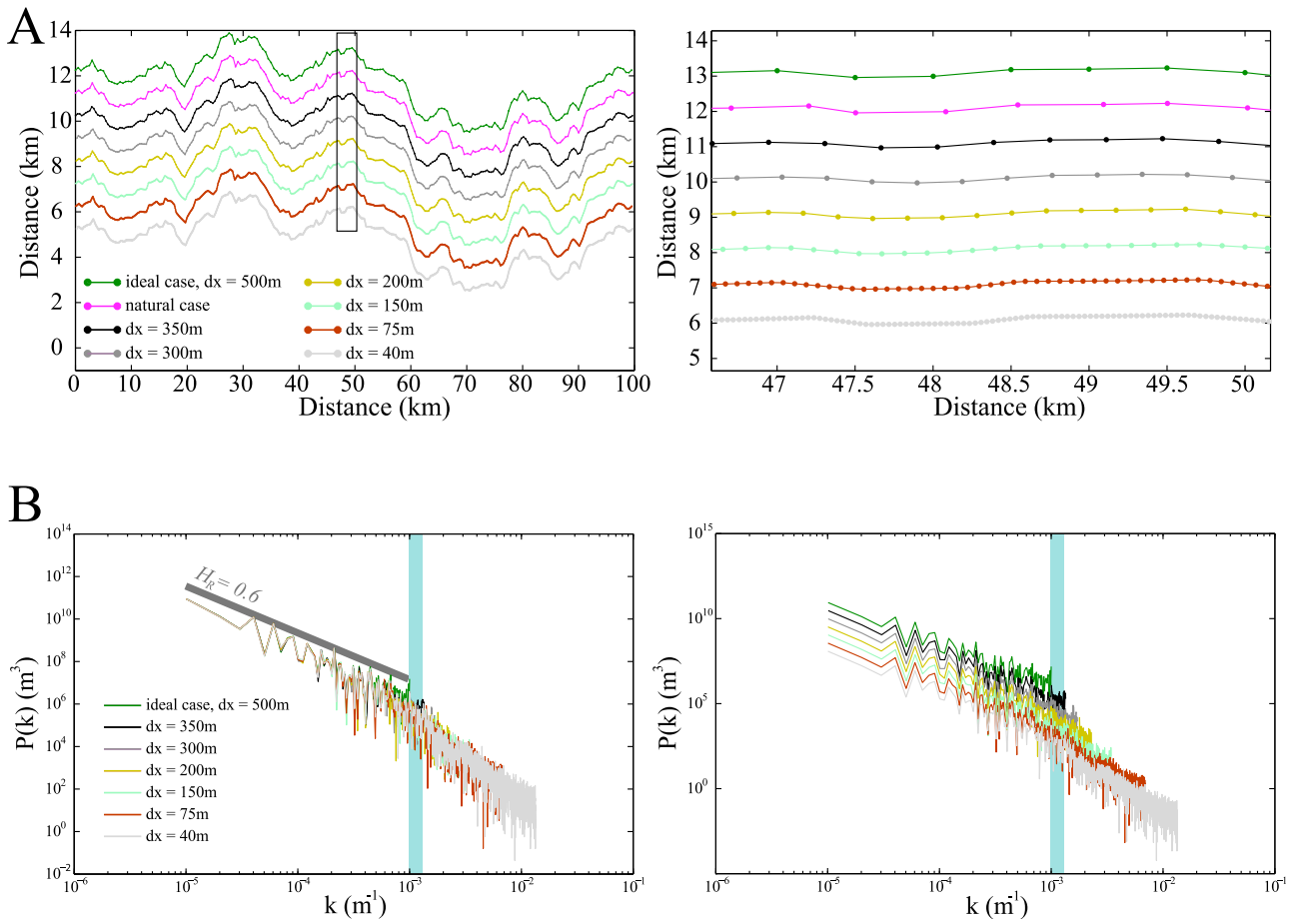

Figure A4. Effect of re-sampling on synthetic self-affine profiles. (a) Example of synthetic rough profiles with a standard deviation that scales as $RMS = 0.01\ L^{0.6}$, analogue of digitized surface rupture traces. The green profile at the top of the left figure is the original ideal synthetic profile with a regular point spacing δx of 500 m. A Gaussian white noise perturbation with a distribution [0, 250 m] is added on the original regular spacing to obtain a noisy profile (pink curve) similar to that of original ruptures maps. This noisy synthetic profile with irregular point spacing is re-sampled with a regular spacing δx. The inset zooms on the synthetic profiles located on the right. (b) Fourier power spectra of the synthetic self-affine profiles shown in Figure A4a. Colors of each curves correspond to those of profiles. On the right the spectra have been shifted vertically to improve the visibility.

perturbation with a distribution of [0, 250 m] (Figure A4). This altered profile is re-sampled with different values of δx in the range [40–350] m. The Fourier spectra (Figure A4) indicate that for the different values of δx, the large scale regime (above 750 m) characterizing the input self-affine behavior with a Hurst exponent of 0.6 is not biased. This test validates that the re-sampling procedure makes it possible to keep the scaling information of the rupture traces at spatial scales above 1200 m.

[63] **Acknowledgments.** This study was supported by the Agence Nationale pour la Recherche grant ANR-JCJC-0011-01, ANR ECCO TRIGGERLAND, ANR RiskNat SUPNAF, and a Fulbright fellowship. Field work was supported in part by NSF grant EAR-0711575. The authors are very grateful to Michel Bouchon, Anne-Marie Boullier, Jean-Pierre Gratier, David Marsan, and Fabrice Cotton for encouragements and scientific stimulations. William L. Power is thanked for his detailed and constructive comments on an early version of this work. The authors gratefully acknowledge Andrew P. Rathbun and Megan Avants for their constructive comments that helped to improve the content and clarity of the manuscript and James D. Kirkpatrick for fruitful discussions.

References

Alava, M. J., P. K. V. V. Nukala, and S. Zapperi (2006), Statistical models of fracture, *Adv. Phys.*, *55*(3–4), 349–476, doi:10.1080/00018730300741518.

Angheluta, L., T. Candela, J. Mathiesen, and F. Renard (2011), Effect of surface morphology on the dissipation during shear and slip along a rock-rock interface that contains a visco-elastic core, *Pure Appl. Geophys.*, *168*, 2335–2344, doi:10.1007/s00024-011-0272-8.

Aochi, H., and R. Madariaga (2003), The 1999 Izmit, Turkey, Earthquake: Nonplanar fault structure, dynamic rupture process, and strong ground motion, *Bull. Seismol. Soc. Am.*, *93*, 1249–1266, doi:10.1785/0120020167.

Atkinson, B. (1991), *Fracture Mechanics of Rock*, Academic, San Diego, California.

Avouac, J.-P., F. Ayoub, S. Leprince, O. Konca, and D. V. Helmberger (2006), The 2005, Mw 7.6 Kashmir earthquake: Sub-pixel correlation of ASTER images and seismic waveforms analysis, *Earth Planet. Sci. Lett.*, *249*, 514–528, doi:10.1016/j.epsl.2006.06.025.

Barabási, A.-L., and H. E. Stanley (1995), *Fractal Concepts in Surface Growth*, Cambridge Univ. Press, New York, doi:10.1017/CBO9780511599798.

Barka, A. (1996), Slip distribution along the North Anatolian Fault associated with the large earthquakes of the period 1939 to 1967, *Bull. Seismol. Soc. Am.*, *86*, 1238–1254.

Beanland, S., and M. Clark (1994), The Owens Valley fault zone, eastern California, and surface rupture associated with the 1872 earthquake, *U.S. Geol. Surv. Bull.*, *1982*, 29 pp.

Bendat, J. S., and A. G. Piersol (1986), *Random Data: Analysis and Measurement Procedures*, 566 pp., John Wiley, New York.

Ben-Zion, Y., and C. G. Sammis (2003), Characterization of fault zones, *Pure Appl. Geophys.*, *160*, 677–715, doi:10.1007/PL00012554.

Berberian, M., J. A. Jackson, M. Qorashi, M. M. Khatib, K. Priestley, M. Talebian, and M. Ghafuri-Ashtiani (1999), The 1997 May 10 Zirkuh (Qa'enat) earthquake (Mw 7.2): Faulting along the Sistan suture zone of eastern Iran, *Geophys. J. Int.*, *136*, 671–694, doi:10.1046/j.1365-246x.1999.00762.x.

Berg, S. S. (2004), The architecture of normal fault zones in sedimentary rocks: Analysis of fault composition, damage zone asymmetry, and multi-phase flow properties, PhD thesis, 118 pp., Univ. of Bergen, Bergen, Norway.

Bhat, H., R. Dmowska, J. Rice, and N. Kame (2004), Dynamic slip transfer from the Denali to Totschunda faults, Alaska: Testing theory for fault branching, *Bull. Seismol. Soc. Am.*, *94*(6B), S202–S213, doi:10.1785/0120040601.

Bistacchi, A., M. Massironi, and L. Menegon (2010), Three-dimensional characterization of a crustal-scale fault zone: The Pusteria and Sprechenstein fault system (eastern Alps), *J. Struct. Geol.*, *32*, 2022–2041, doi:10.1016/j.jsg.2010.06.003.

Bistacchi, A., W. A. Griffith, S. A. Smith, G. di Toro, R. Jones, and S. Nielsen (2011), Fault roughness at seismogenic depths from LIDAR and photogrammetric analysis, *Pure Appl. Geophys.*, *168*, 2345–2363, doi:10.1007/s00024-011-0301-7.

Bonamy, D., and E. Bouchaud (2011), Failure of heterogeneous materials: A dynamic phase transition?, *Phys. Rep.*, *498*, 1–44, doi:10.1016/j.physrep.2010.07.006.

Bouchaud, E. (1997), Scaling properties of cracks, *J. Phys. Condens. Matter*, *9*, 4319–4344, doi:10.1088/0953-8984/9/21/002.

Bouchaud, E., G. Lapasset, and J. Planès (1990), Fractal dimension of fractured surfaces: A universal value?, *Europhys. Lett.*, *13*, 73–79.

Bouchon, M. (1997), The state of stress on some faults of the San Andreas system as inferred from near field strong motion data, *J. Geophys. Res.*, *102*, 11,731–11,744, doi:10.1029/97JB00623.

Bouchon, M., H. Karabulut, M.-P. Bouin, J. Schmittbuhl, M. Vallée, R. Archuleta, S. Das, F. Renard, and D. Marsan (2010), Faulting characteristics of supershear earthquakes, *Tectonophysics*, *493*, 244–253, doi:10.1016/j.tecto.2010.06.011.

Brodsky, E. E., J. G. Gilchrist, A. Sagy, and C. Colletini (2011), Faults smooth gradually as a function of slip, *Earth Planet. Sci. Lett.*, *302*, 185–193, doi:10.1016/j.epsl.2010.12.010.

Brown, S. R., and C. H. Scholz (1985), Broad bandwidth study of the topography of natural rock surfaces, *J. Geophys. Res.*, *90*, 12,575–12,582, doi:10.1029/JB090iB14p12575.

Burchfiel, B. C., Z. Peizhen, W. Yipeng, Z. Weiqi, S. Fangmin, D. Qidong, P. Molnar, and L. Royden (1991), Geology of the Haiyuan fault zone, Ningxia-Hui autonomous region, China, and its relation to the evolution of the northeastern margin of the Tibetan plateau, *Tectonics*, *10*, 1091–1110, doi:10.1029/90TC02685.

Candela, T., F. Renard, M. Bouchon, D. Marsan, J. Schmittbuhl, and C. Voisin (2009), Characterization of fault roughness at various scales: Implications of three-dimensional high resolution topography measurements, *Pure Appl. Geophys.*, *166*, 1817–1851, doi:10.1007/s00024-009-0521-2.

Candela, T., F. Renard, J. Schmittbuhl, M. Bouchon, and E. E. Brodsky (2011a), Fault slip distribution and fault roughness, *Geophys. J. Int.*, *187*, 959–968, doi:10.1111/j.1365-246X.2011.05189.x.

Candela, T., F. Renard, M. Bouchon, J. Schmittbuhl, and E. E. Brodsky (2011b), Stress drop during earthquakes: Effect of fault roughness scaling, *Bull. Seismol. Soc. Am.*, *101*, 2369–2387, doi:10.1785/0120100298.

Carcaillet, J., I. Manighetti, C. Chauvel, A. Schlagenhauf, and J. M. Nicole (2008), Identifying past earthquakes on an active normal fault (Magnola, Italy) from the chemical analysis of its exhumed carbonate fault plane, *Earth Planet. Sci. Lett.*, *271*, 145–158, doi:10.1016/j.epsl.2008.03.059.

Chen, G., and H. A. Spetzler (1993), Topographic characteristics of laboratory-induced shear fractures, *Pure Appl. Geophys.*, *140*, 123–135, doi:10.1007/BF00876874.

Chen, Y.-G., W.-S. Chen, J.-C. Lee, Y.-H. Lee, C.-T. Lee, H.-C. Chang, and C.-H. Lo (2001), Surface rupture of 1999 Chi-Chi earthquake yields insights on active tectonics of central Taiwan, *Bull. Seismol. Soc. Am.*, *91*(5), 977–985, doi:10.1785/0120000721.

Chester, F. M., and J. S. Chester (2000), Stress and deformation along wavy frictional faults, *J. Geophys. Res.*, *105*, 23,421–23,430, doi:10.1029/2000JB900241.

Chester, J. S., and R. C. Fletcher (1997), Stress distribution and failure in anisotropic rock near a bend on a weak fault, *J. Geophys. Res.*, *102*, 693–708, doi:10.1029/96JB02791.

Christensen, M. (2004), Soft sediment faulting–Investigation of the 3D geometry and fault zone properties, PhD thesis, 146 pp., Univ. of Aarhus, Aarhus, Denmark.

Clausen, J. A., R. H. Gabrielsen, and E. Johnsen (2003), Fault architecture and clay smear distribution: Examples from field studies and drained ring-shear experiments, *Norweg. J. Geol.*, *83*(2), 131–146.

Crone, A. J., and M. N. Machette (1984), Surface faulting accompanying the Borah Peak earthquake, central Idaho, *Geology*, *12*, 664–667, doi:10.1130/0091-7613(1984)12<664:SFATBP>2.0.CO;2.

Dieterich, J. H., and D. E. Smith (2009), Nonplanar faults: Mechanics of slip and off-fault damage, *Pure Appl. Geophys.*, *166*, 1799–1815, doi:10.1007/s00024-009-0517-y.

Doser, D. I. (1986), Earthquake processes in the Rainbow Mountain-Fairview Peak-Dixie Valley, Nevada, region 1954–1969, *J. Geophys. Res.*, *91*, 12,572–12,586, doi:10.1029/JB091iB12p12572.

Dunham, E. M., D. Belanger, L. Cong, and J. E. Kozdon (2011), Earthquake ruptures with strongly rate-weakening friction and off-fault plasticity: 2: Nonplanar faults, *Bull. Seismol. Soc. Am.*, *101*(5), 2308–2322, doi:10.1785/0120100076.

Dysthe, D. K., Y. Podladchikov, F. Renard, J. Feder, and B. Jamtveit (2002), Universal scaling in transient creep, *Phys. Rev. Lett.*, *89*, 246102, doi:10.1103/PhysRevLett.89.246102.

Faulkner, D. R., C. A. L. Jackson, R. J. Lunn, R. W. Schlische, Z. K. Shipton, C. A. J. Wibberley, and M. O. Withjack (2010), A review of recent developments concerning the structure, mechanics and fluid properties of fault zones, *J. Struct. Geol.*, *32*, 1557–1575, doi:10.1016/j.jsg.2010.06.009.

Feder, J. (1988), *Fractals*, Plenum, New York.

Florensov, N. A., and V. P. Solonenko (1965), *The Gobi-Altai Earthquake*, 424 pp., U.S. Dep. of Commer., Washington, D. C.

Fu, B., P. Shi, H. Guo, S. Okuyama, Y. Ninomiya, and S. Wright (2011), Surface deformation related to the 2008 Wenchuan earthquake, and mountain building of the Longmen Shan, eastern Tibetan Plateau, *J. Asian Earth Sci.*, *40*(4), 805–824, doi:10.1016/j.jseaes.2010.11.011.

Gabrielsen, R. H., and J. A. Clausen (2001), Horses and duplexes in extensional regimes: A scale-modeling contribution, in *Tectonic Models: A Volume in Honor of Hans Ramberg*, edited by H. A. Koyi and N. Mancktelow, *Mem. Geol. Soc. Am.*, *193*, 207–220, doi:10.1130/0-8137-1193-2.207.

Gao, H., and J. Rice (1986), Shear-stress intensity factors for a planar crack with slightly curved front, *J. Appl. Mech.*, *53*(4), 774–778.

Gao, H., J. Rice, and J. Lee (1991), Penetration of a quasi-statically slipping crack into a seismogenic zone of heterogeneous fracture-resistance, *J. Geophys. Res.*, *96*, 21,535–21,548.

Gaudemer, Y., P. Tapponnier, B. Meyer, G. Peltzer, S. Guo, Z. Chen, H. Dai, and I. Cifuentes (1995), Partitioning of crustal slip between linked active faults in the eastern Qilian Shan, and evidence for a major seismic gap, the "Tianzhu gap", on the western Haiyuan fault, Gansu (China), *Geophys. J. Int.*, *120*, 599–645, doi:10.1111/j.1365-246X.1995.tb01842.x.

Gibbs, A. D. (1983), Balanced cross-section construction from seismic sections in areas of extensional tectonics, *J. Struct. Geol.*, *5*, 153–160, doi:10.1016/0191-8141(83)90040-8.

Gibbs, A. D. (1984), Structural evolution of extensional margins, *J. Geol. Soc.*, *141*, 609–620, doi:10.1144/gsjgs.141.4.0609.

Griffith, W. A., S. Nielsen, G. di Toro, and S. A. F. Smith (2010), Rough faults, distributed weakening, and off-fault deformation, *J. Geophys. Res.*, *115*, B08409, doi:10.1029/2009JB006925.

Hansen, A., and J. Schmittbuhl (2003), Origin of the universal roughness exponent of brittle fracture surfaces: Stress-weighted percolation in the damage zone, *Phys. Rev. Lett.*, *90*(4), 045504, doi:10.1103/PhysRevLett.90.045504.

Hubert-Ferrari, A., R. Armijo, G. King, B. Meyer, and K. Barka (2002), Morphology, displacement, and slip rates along the North Anatolian Fault, Turkey, *J. Geophys. Res.*, *107*(B10), 2235, doi:10.1029/2001JB000393.

Hussain, A., and R. S. Yeats (2009), MonaLisa, 2009: Geological setting of the 8 October 2005 Kashmir earthquake, *J. Seismol.*, *13*, 315–325, doi:10.1007/s10950-008-9101-7.

Jachens, R. C., V. E. Langenheim, and J. C. Matti (2002), Relationship of the 1999 Hector Mine and 1992 Landers fault ruptures to offsets on neogene faults and distribution of late cenozoic basins in the eastern California shear zone, *Bull. Seismol. Soc. Am.*, *92*, 1592–1605, doi:10.1785/0120000915.

Johnson, A. M., and R. C. Fletcher (1994), *Folding of Viscous Layers*, 461 pp., Columbia Univ. Press, New York.

Kaneda, H., et al. (2008), Surface rupture of the 2005 Kashmir, Pakistan, earthquake, and its active tectonic implications, *Bull. Seismol. Soc. Am.*, *98*, 521–557, doi:10.1785/0120070073.

Karig, D. E. (1983), Accreted terranes in the Northern part of the Philippine archipelago, *Tectonics*, *2*, 211–236, doi:10.1029/TC002i002p00211.

Klinger, Y. (2010), Relation between continental strike-slip earthquake segmentation and thickness of the crust, *J. Geophys. Res.*, *115*, B07306, doi:10.1029/2009JB006550.

Klinger, Y., X. W. Xu, P. Tapponnier, J. Van der Woerd, C. Lasserre, and G. King (2005), High-resolution satellite imagery mapping of the surface rupture and slip distribution of the Mw 7.8, 14 November 2001 Kokoxili earthquake, Kunlun Fault, northern Tibet, China, *Bull. Seismol. Soc. Am.*, *95*(5), 1970–1987, doi:10.1785/0120040233.

Klinger, Y., R. Michel, and G. C. P. King (2006), Evidence for an earthquake barrier model from Mw similar to 7.8 Kokoxili (Tibet) earthquake slip-distribution, *Earth Planet. Sci. Lett.*, *242*(3–4), 354–364, doi:10.1016/j.epsl.2005.12.003.

Kondo, H., Y. Awata, Ö. Emre, A. Doğan, S. Özalp, F. Tokay, C. Yıldırım, T. Yoshioka, and K. Okumura (2005), Slip distribution, fault geometry, and fault segmentation of the 1944 Bolu-Gerede earthquake rupture, North Anatolian Fault, Turkey, *Bull. Seismol. Soc. Am.*, *95*, 1234–1249, doi:10.1785/0120040194.

Kondo, H., V. Özaksoy, and C. Yıldırım (2010), Slip history of the 1944 Bolu-Gerede earthquake rupture along the North Anatolian fault system: Implications for recurrence behavior of multisegment earthquakes, *J. Geophys. Res.*, *115*, B04316, doi:10.1029/2009JB006413.

Kumahara, Y., and T. Nakata (2006), Active faults in the epicentral area of the 2005 Pakistan earthquake, *Spec. Publ., 41*, 54 pp., Res. Cent. for Reg. Geogr., Hiroshima Univ., Hiroshima, Japan.

Kurushin, R. A., A. Bayasgalan, M. Ölziybat, B. Enhtuvshin, P. Molnar, C. Bayarsayhan, K. Hudnut, and L. Jian (1997), The surface rupture of the 1957 Gobi-Altay, Mongolia, earthquake. *Spec. Pap. Geol. Soc. Am.*, *320*, 142 pp.

Lee, J. J., and R. L. Bruhn (1996), Structural anisotropy of normal fault surfaces, *J. Struct. Geol.*, *18*, 1043–1059, doi:10.1016/0191-8141(96)00022-3.

Mai, P. M., and G. C. Beroza (2002), A spatial random field model to characterize complexity in earthquake slip, *J. Geophys. Res.*, *107*(B11), 2308, doi:10.1029/2001JB000588.

Mandelbrot, B. B. (1983), *The Fractal Geometry of Nature*, 468 pp., Freeman, New York.

Manighetti, I., M. Campillo, S. Bouley, and F. Cotton (2007), Earthquake scaling, fault segmentation, and structural maturity, *Earth Planet. Sci. Lett.*, *253*(3–4), 429–438, doi:10.1016/j.epsl.2006.11.004.

Meakin, P. (1998), *Fractals: Scaling and Growth far From Equilibrium*, Cambridge Univ. Press, New York.

Méheust, Y. (2002), Ecoulements dans les fractures ouvertes, PhD thesis, Univ. Paris VI, Paris.

Mitchell, A. H. G., F. Hernandez, and A. P. dela Cruz (1986), Cenozoic evolution of the Philippine archipelago, *J. Southeast Asian Earth Sci.*, *1*, 3–22, doi:10.1016/0743-9547(86)90003-6.

Mitchell, T. M., and D. R. Faulkner (2009), The nature and origin of off-fault damage surrounding strike-slip fault zones with a wide range of displacements: A field study from the Atacama fault system, northern Chile, *J. Struct. Geol.*, *31*(8), 802–816, doi:10.1016/j.jsg.2009.05.002.

Myers, W. B., and W. Hamilton (1964), Deformation accompanying the Hebgen Lake earthquake of August 17, 1959, in *The Hebgen Lake, Montana Earthquake of August 17, 1959*, *U.S. Geol. Surv. Prof. Pap.*, *435*, 55–98.

Nielsen, S. B., and L. Knopoff (1998), The equivalent strength of geometrical barriers to earthquakes, *J. Geophys. Res.*, *103*, 9953–9965, doi:10.1029/97JB03293.

Okaya, D. A., and G. A. Thompson (1985), Geometry of Cenozoic extensional faulting: Dixie Valley, Nevada, *Tectonics*, *4*, 107–125, doi:10.1029/TC004i001p00107.

Palumbo, L., L. Benedetti, D. Bourles, A. Cinque, and R. Finkel (2004), Slip history of the Magnola fault (Apennines, central Italy) from 36Cl surface exposure dating: Evidence for strong earthquakes over the Holocene, *Earth Planet. Sci. Lett.*, *225*, 163–176, doi:10.1016/j.epsl.2004.06.012.

Poliakov, A. N., R. Dmowska, and J. R. Rice (2002), Dynamic shear rupture interactions with fault bends and off-axis secondary faulting, *J. Geophys. Res.*, *107*(B11), 2295, doi:10.1029/2001JB000572.

Power, W. L., and W. B. Durham (1997), Topography of natural and artificial fractures in granitic rocks: Implications for studies of rock friction and fluid migration, *Int. J. Rock Mech. Min. Sci.*, *34*, 979–989, doi:10.1016/S1365-1609(97)80007-X.

Power, W. L., and T. E. Tullis (1989), The relationship between slickenside surfaces in fine-grained quartz and the seismic cycle, *J. Struct. Geol.*, *11*, 879–893, doi:10.1016/0191-8141(89)90105-3.

Power, W. L., and T. E. Tullis (1991), Euclidean and fractal models for the description of rock surface roughness, *J. Geophys. Res.*, *96*, 415–424, doi:10.1029/90JB02107.

Power, W. L., and T. E. Tullis (1992), The contact between opposing fault surfaces at Dixie Valley, Nevada, and implications for fault mechanics, *J. Geophys. Res.*, *97*, 15,425–15,435, doi:10.1029/92JB01059.

Power, W. L., T. E. Tullis, S. R. Brown, G. N. Boitnott, and C. H. Scholz (1987), Roughness of natural fault surfaces, *Geophys. Res. Lett.*, *14*, 29–32, doi:10.1029/GL014i001p00029.

Press, W. H., S. A. Teukolsky, W. T. Vetterling, and B. P. Flannery (2007), *Numerical Recipes*, 3rd ed., Cambridge Univ. Press, Cambridge, U. K.

Renard, F., C. Voisin, D. Marsan, and J. Schmittbuhl (2006), High resolution 3D laser scanner measurements of a strike-slip fault quantify its morphological anisotropy at all scales, *Geophys. Res. Lett.*, *33*, L04305, doi:10.1029/2005GL025038.

Resor, P. G., and V. E. Meer (2009), Slip heterogeneity on a corrugated fault, *Earth Planet. Sci. Lett.*, *288*, 483–491, doi:10.1016/j.epsl.2009.10.010.

Ringenbach, J. C., N. Pinet, J. F. Stephan, and J. Delteil (1993), Structural variety and tectonic evolution of strike-slip basins related to the Philippine fault system, northern Luzon, Philippines, *Tectonics*, *12*, 187–203, doi:10.1029/92TC01968.

Sagy, A., E. E. Brodsky, and G. J. Axen (2007), Evolution of fault-surface roughness with slip, *Geology*, *35*, 283–286, doi:10.1130/G23235A.1.

Savage, H. M., and E. E. Brodsky (2011), Collateral damage: Capturing fault strand formation in fracture profiles, *J. Geophys. Res.*, *116*, B03405, doi:10.1029/2010JB007665.

Schmittbuhl, J., S. Gentier, and R. Roux (1993), Field measurements of the roughness of fault surfaces, *Geophys. Res. Lett.*, *20*, 639–641, doi:10.1029/93GL00170.

Schmittbuhl, J., F. Schmitt, and C. H. Scholz (1995a), Scaling invariance of crack surfaces, *J. Geophys. Res.*, *100*, 5953–5973, doi:10.1029/94JB02885.

Schmittbuhl, J., J. Vilotte, and S. Roux (1995b), Reliability of self-affine measurements, *Phys. Rev. E*, *51*, 131–147, doi:10.1103/PhysRevE.51.131.

Schmittbuhl, J., A. Delaplace, K. Maloy, H. Perfettini, and J. Vilotte (2003), Slow crack propagation and slip correlations, *Pure Appl. Geophys.*, *160*, 961–976, doi:10.1007/PL00012575.

Schmittbuhl, J., G. Chambon, A. Hansen, and M. Bouchon (2006), Are stress distributions along faults the signature of asperity squeeze?, *Geophys. Res. Lett.*, *33*, L13307, doi:10.1029/2006GL025952.

Schmittbuhl, J., A. Steyer, L. Jouniaux, and R. Toussaint (2008), Fracture morphology and viscous transport, *Int. J. Rock Mech. Min. Sci.*, *45*, 422–430, doi:10.1016/j.ijrmms.2007.07.007.

Sharp, R. V. (1967), San Jacinto Fault zone in the peninsular ranges of Southern California, *Geol. Soc. Am. Bull.*, *78*, 705–730, doi:10.1130/0016-7606(1967)78[705:SJFZIT]2.0.CO;2.

Sylvester, A. G. (1988), Strike-slip faults, *Geol. Soc. Am. Bull.*, *100*, 1666–1703, doi:10.1130/0016-7606(1988)100<1666:SSF>2.3.CO;2.

Thouvenot, F. (1998), The ML 5.3 Epagny (French Alps) earthquake of 1996 July 15: A long-awaited event on the Vuache Fault, *Geophys. J. Int.*, *135*, 876–892, doi:10.1046/j.1365-246X.1998.00662.x.

Vallée, M., M. Landès, N. M. Shapiro, and Y. Klinger (2008), The 14 November 2001 Kokoxili (Tibet) earthquake: High-frequency seismic radiation originating from the transition between sub-Rayleigh and supershear rupture velocity regimes, *J. Geophys. Res.*, *113*, B07305, doi:10.1029/2007JB005520.

van Gent, H. W., B. Stefan, J. L. Urai, P. A. Kukla, and K. Reicherter (2009), Paleostresses of the Groningen area, the Netherlands—Results of a seismic based structural reconstruction, *Tectonophysics*, *470*, 147–161, doi:10.1016/j.tecto.2008.09.038.

Voisin, C., F. Renard, and J.-R. Grasso (2007), Long term friction: From stick-slip to stable sliding, *Geophys. Res. Lett.*, *34*, L13301, doi:10.1029/2007GL029715.

Wallace, R. E., and R. A. Whitney (1984), Late Quaternary history of the Stillwater Seismic Gap, Nevada, *Bull. Seismol. Soc. Am.*, *74*, 301–314.

Wei, S., et al. (2011), Superficial simplicity of the 2010 El Mayor-Cucapah earthquake of Baja California in Mexico, *Nat. Geosci.*, *201*, 1–4, doi:10.1038/ngeo1213.

Wei, Z., H. He, F. Shi, X. Gao, and C. Xu (2010), Topographic characteristics of rupture surface associated with the Wenchuan earthquake of Mw7.9, in May 12, 2008, *Bull. Seismol. Soc. Am.*, *100*, 2669–2680, doi:10.1785/0120090260.

Wesnousky, S. G. (1988), Seismological and structural evolution of strike-slip faults, *Nature*, *335*, 340–343, doi:10.1038/335340a0.

Wesnousky, S. G. (2006), Predicting the endpoints of earthquake ruptures, *Nature*, *444*(7117), 358–360, doi:10.1038/nature05275.

Wesnousky, S. G. (2008), Displacement and geometrical characteristics of earthquake surface ruptures: Issues and implications for seismic-hazard

analysis and the process of earthquake rupture, *Bull. Seismol. Soc. Am.*, *98*, 1609–1632, doi:10.1785/0120070111.

Witkind, I. J. (1964), Reactivated faults north of Hebgen Lake, *U.S. Geol. Surv. Prof. Pap.*, *435-G*, 37–50.

Xu, X., X. Wen, G. Yu, G. Chen, Y. Klinger, J. Hubbard, and J. Shaw (2009), Coseismic reverse- and oblique-slip surface faulting generated by the 2008 Mw 7.9 Wenchuan earthquake, China, *Geology*, *37*(6), 515–518, doi:10.1130/G25462A.1.

Zhang, W., D. Jiao, P. Zhang, P. Molnar, B. C. Burchfiel, D. Qidong, W. Yipeng, and S. Fangøin (1987), Displacement along the Haiyuan fault associated with the great 1920 Haiyuan, China, earthquake, *Bull. Seismol. Soc. Am.*, *77*, 117–131.